Modeling the Launch Abort Vehicle's Subsonic Aerodynamics from Free Flight Testing

Christopher L. Hartman
National Institute of Aerospace, Hampton, Virginia

NASA STI Program . . . in Profile

Since its founding, NASA has been dedicated to the advancement of aeronautics and space science. The NASA scientific and technical information (STI) program plays a key part in helping NASA maintain this important role.

The NASA STI program operates under the auspices of the Agency Chief Information Officer. It collects, organizes, provides for archiving, and disseminates NASA's STI. The NASA STI program provides access to the NASA Aeronautics and Space Database and its public interface, the NASA Technical Report Server, thus providing one of the largest collections of aeronautical and space science STI in the world. Results are published in both non-NASA channels and by NASA in the NASA STI Report Series, which includes the following report types:

- TECHNICAL PUBLICATION. Reports of completed research or a major significant phase of research that present the results of NASA programs and include extensive data or theoretical analysis. Includes compilations of significant scientific and technical data and information deemed to be of continuing reference value. NASA counterpart of peer-reviewed formal professional papers, but having less stringent limitations on manuscript length and extent of graphic presentations.

- TECHNICAL MEMORANDUM. Scientific and technical findings that are preliminary or of specialized interest, e.g., quick release reports, working papers, and bibliographies that contain minimal annotation. Does not contain extensive analysis.

- CONTRACTOR REPORT. Scientific and technical findings by NASA-sponsored contractors and grantees.

- CONFERENCE PUBLICATION. Collected papers from scientific and technical conferences, symposia, seminars, or other meetings sponsored or co-sponsored by NASA.

- SPECIAL PUBLICATION. Scientific, technical, or historical information from NASA programs, projects, and missions, often concerned with subjects having substantial public interest.

- TECHNICAL TRANSLATION. English-language translations of foreign scientific and technical material pertinent to NASA's mission.

Specialized services also include creating custom thesauri, building customized databases, and organizing and publishing research results.

For more information about the NASA STI program, see the following:

- Access the NASA STI program home page at *http://www.sti.nasa.gov*

- E-mail your question via the Internet to help@sti.nasa.gov

- Fax your question to the NASA STI Help Desk at 443-757-5803

- Phone the NASA STI Help Desk at 443-757-5802

- Write to:
  NASA STI Help Desk
  NASA Center for AeroSpace Information
  7115 Standard Drive
  Hanover, MD 21076-1320

NASA/CR–2010-216837

Modeling the Launch Abort Vehicle's Subsonic Aerodynamics from Free Flight Testing

Christopher L. Hartman
National Institute of Aerospace, Hampton, Virginia

August 2010

Acknowledgments

I would like to thank my graduate advisor Dr. Andre Mazzoleni. Dr. Mazzoleni has been a very helpful guide through my graduate career. He helped me gain initial funding at the National Institute of Aerospace and NASA.

I would like to thank Dr. Tolson at the National Institute of Aerospace for his help in reviewing and discussing my research. He has been an invaluable resource as an academic and research advisor.

I would like to thank Dr. Eugene Morelli and Steve Derry, my technical advisors at NASA, for providing an insight into practical analysis.

I would like to thank Mike Fremaux and Bruce Owens for allowing me to take part in the LAV Vertical Spin Tunnel research. I would also like to thank Mike and Bruce for their help in providing data for this experiment, and additional wind tunnel and aerodynamics data for comparison.

Finally, I would like to thank Carey Buttrill and the Dynamic Systems and Controls Branch at NASA Langley Research Center. Thank you for allowing me to pursue my research and for providing an excellent work environment.

Abstract

An investigation into the aerodynamics of the Launch Abort Vehicle for NASA's Constellation Crew Launch Vehicle in the subsonic, incompressible flow regime was conducted in the NASA Langley 20-ft Vertical Spin Tunnel. Time histories of center of mass position and Euler Angles are captured using photogrammetry. Time histories of the wind tunnel's airspeed and dynamic pressure are recorded as well. The primary objective of the investigation is to determine models for the aerodynamic yaw and pitch moments that provide insight into the static and dynamic stability of the vehicle. System IDentification Programs for AirCraft is used to determine the aerodynamic model structure and estimate model parameters. Aerodynamic models for the aerodynamic body Y and Z force coefficients, and the pitching and yawing moment coefficients were identified.

Contents

List of Tables

List of Figures

iii

Nomenclature

C_l Aerodynamic rolling moment coefficient.

C_m Aerodynamic pitching moment coefficient.

C_n Aerodynamic yawing moment coefficient.

C_X Body x-axis aerodynamic force coefficient.

C_Y Body y-axis aerodynamic force coefficient.

C_Z Body z-axis aerodynamic force coefficient.

$[C]$ Direction cosine matrix.

F_0 Partial F statistic.

$\mathbf{H}$ Matrix of system input measurements.

I_{xx} X-axis Moment of Inertia, kg-m^2.

I_{xy} Product of Inertia between X and Y axes, kg-m^2.

I_{xz} Product of Inertia between X and Z axes, kg-m^2.

I_{yy} Y-axis Moment of Inertia, kg-m^2.

I_{yz} Product of Inertia between Y and Z axes, kg-m^2.

I_{zz} Z-axis Moment of Inertia, kg-m^2.

L Reference Length, m.

M Mach Number.

m Mass, kg.

p X component of angular velocity in body coordinate system, rad/sec.

$\dot{p}$ X component of angular acceleration in the body coordinate system, rad/sec/sec.

q Y component of angular velocity in body coordinate system, rad/sec.

$\bar{q}$ Dynamic pressure in the tunnel, Pa.

$\dot{q}$ Y component of angular acceleration in body coordinate system, rad/sec/sec.

r Z component of angular velocity in body coordinate system, rad/sec.

R^2 Coefficient of Determination

$\dot{r}$ Z component of angular velocity of model in body coordinate system, rad/sec/sec.

Re Reynolds Number.

S Reference Area, m^2.

t Time, sec.

$[T]$ Kinematic transform matrix.

u X component of velocity in body coordinate system, m/sec.

u'	X component of relative wind in body coordinate system, m/sec.
V	Wind airspeed in the tunnel, m/sec.
v	Y component of velocity in body coordinate system, m/sec.
v'	Y component of relative wind in body coordinate system, m/sec.
w	Z component of velocity in body coordinate system, m/sec.
w'	Z component of relative wind in body coordinate system, m/sec.
X	X position in tunnel coordinate system, m.
$\mathbf{x}$	Vector of unknown constant parameters.
$\ddot{X}$	X component of acceleration in tunnel coordinate system, m/sec/sec.
$\dot{X}$	X component of velocity in tunnel coordinate system, m/sec.
Y	Y Position in tunnel coordinate system, m.
$\ddot{Y}$	Y component of acceleration in tunnel coordinate system, m/sec/sec.
$\dot{Y}$	Y component of velocity in tunnel coordinate system, m/sec.
Z	Z Position in tunnel coordinate system, m.
$\mathbf{z}$	Vector of output measurements.
$\ddot{Z}$	Z component of acceleration in tunnel coordinate system, m/sec/sec.
$\dot{Z}$	Z component of velocity in tunnel coordinate system, m/sec.
α	Angle of Attack, rad.
α_T	Total Angle of Attack, rad.
β	Sideslip Angle, rad.
$\mathbf{\Gamma}_x$	Covariance of parameter estimates $\mathbf{x}$.
ν	Vector of measurement noise.
ϕ	Roll Euler angle, rad.
ϕ_A	Aerodynamic clock angle, rad.
$\dot{\phi}$	Time derivative of roll Euler angle, rad/sec.
ψ	Yaw Euler angle, rad.
$\dot{\psi}$	Time derivative of yaw Euler angle, rad/sec.
θ	Pitch Euler angle, rad.
$\dot{\theta}$	Time derivative of pitch Euler angle, rad/sec.

List of Acronyms

6DOF Six Degrees-of-Freedom

BCS Body Coordinate System

CEV Crew Exploration Vehicle

CLV Crew Launch Vehicle

CM Center of Mass

DAS Data Acquisition System

DCM Direction Cosine Matrix

DFT Discrete Fourier Transform

ESAS Exploration Systems Architecture Study

LES Launch Escape System

LAS Launch Abort System

LAT Launch Abort Tower

LAV Launch Abort Vehicle

LaRC Langley Research Center

MOI Moments of Inertia

MRC Model Reference Center

MSFE Mean Squared Fit Error

NASA National Aeronautics and Space Administration

POI Products of Inertia

SI System International

SIDPAC System IDentification Programs for AirCraft

TCS Tunnel Coordinate System

TDT Transonic Dynamics Tunnel

VST Vertical Spin Tunnel

1 Introduction

In 2004, President Bush [1] outlined a plan for the future exploration of outer space. One of the major objectives of this plan is to return to the moon by 2020. In response to this vision, NASA started to design and develop a new launch system to replace the space shuttle. The architecture for this system is defined in the Exploration Systems Architecture Study (ESAS) final report. [2] The ESAS final report recommended that the new launch system needs a Launch Abort System (LAS) capable of pulling the Crew Exploration Vehicle (CEV)'s Crew Module away from the Crew Launch Vehicle (CLV) during launch failures. While the Launch Abort Vehicle (LAV) (See Figure 1) being developed will incorporate many modern technologies, the concept is similar to the Launch Escape System (LES) utilized during the Mercury and Apollo Programs. [3, 4]
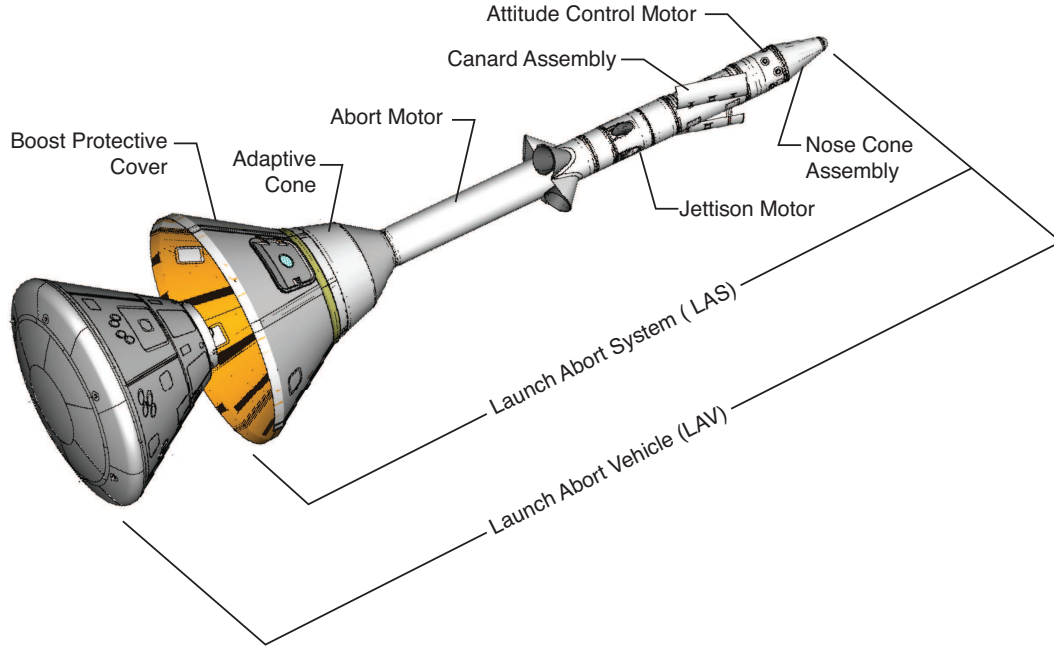
Figure 1. General configuration of Launch Abort Vehicle.

An investigation into the low subsonic aerodynamic stability characteristics of the NASA Orion Launch Abort Vehicle (LAV) was conducted in NASA Langley Research Center (LaRC) 20-foot VST. The goal of this investigation is to model the aerodynamic forces and moments acting on the LAV in the subsonic, incompressible flow regime. The primary objective is to determine models that describe the longitudinal and directional stability of the LAV. A secondary objective is to determine models for the remaining aerodynamic forces and moments.

This investigation focuses on the low-speed (Mach 0.2) heat shield-forward flight of the LAV during a pad abort scenario. During this scenario, the LAV is thrust away from the CLV by an abort motor located in the LAS. The LAV will be flying tower-end forward during this time. The LAV must reorient to a stable heat shield-forward flight state so that the LAS can be jettisoned from the Crew Module to allow for a safe return to the ground. Understanding the LAV's aerodynamic characteristics after reorientation and before LAS jettison when the LAV is at low altitude and speed is critical to ensuring a safely controlled descent.

This investigation was carried out in the NASA LaRC 20-ft VST. A dynamically scaled

model of the LAV was allowed to fly unconstrained inside the wind tunnel. Data analysis was carried out using System IDentification Programs for AirCraft (SIDPAC) [5]. SIDPAC is a collection of software tools developed by Dr. Vladisav Klein and Dr. Eugene Morrelli at National Aeronautics and Space Administration (NASA) LaRC for conducting system identification. The collection consists of different output-error and equation-error estimation algorithms developed for both the time and frequency domains. Additional tools for determining derivatives, Fourier transforms, and data smoothing are also included in SIDPAC. While some of the SIDPAC algorithms are written specifically for aircraft, many of the core algorithms were developed in a generalized form which allows flexability in their implementation. The analysis presented in this report demonstrates how SIDPAC's analysis capabilities can be extended beyond aircraft.

This report documents the approach used to determine the aerodynamic force and moment models. Section 1 describes the scope of the investigation and outlines the report. Section 3 discusses the method used to analyze the collected data. Section 2 discusses the facilities and equipment used to obtain data. Section 4 provides the results of the data analysis and discusses the meaning of the results. Section 5 provides a concluding summary of the report.

2 Experiment

2.1 Test Facilities

The experimental portion of this investigation took place at the NASA LaRC's 20-foot Vertical Spin Tunnel (VST) [6]. The VST has been in use by NASA LaRC since 1941. It has been used to analyze the spin and spin recovery characteristics of many aircraft. This facility has participated in investigations for NASA's Mercury [7], Gemini [8], Apollo [9], Stardust [10–12], and Mars Sample Return [13] missions. Basic research concerning subsonic blunt-bodies [14–16] has been conducted in the VST as well.

Figure 2 depicts a diagram of this VST. The VST is an atmospheric closed-loop, annular return wind tunnel. It features a 12-sided test section that is 20 feet in diameter and 25 feet tall. The test section velocity can be varied from 0 to approximately 85 ft/s. The airflow is produced by a 400 hp DC electric motor with a 3-bladed fixed pitch fan. A tether can be attached to the test article to prevent wall impacts, set initial conditions, and provide quick recovery.

The Tunnel Coordinate System (TCS) depicted in Figure 2 has been adopted as the inertial reference frame for analyzing the test data. The origin is located in the center of the test section. The X-axis is aligned with the central axis of the tunnel pointed toward the floor. The Y-axis and Z-axis are pointed in arbitrary directions with both axes orthogonal with the X-axis and each other.
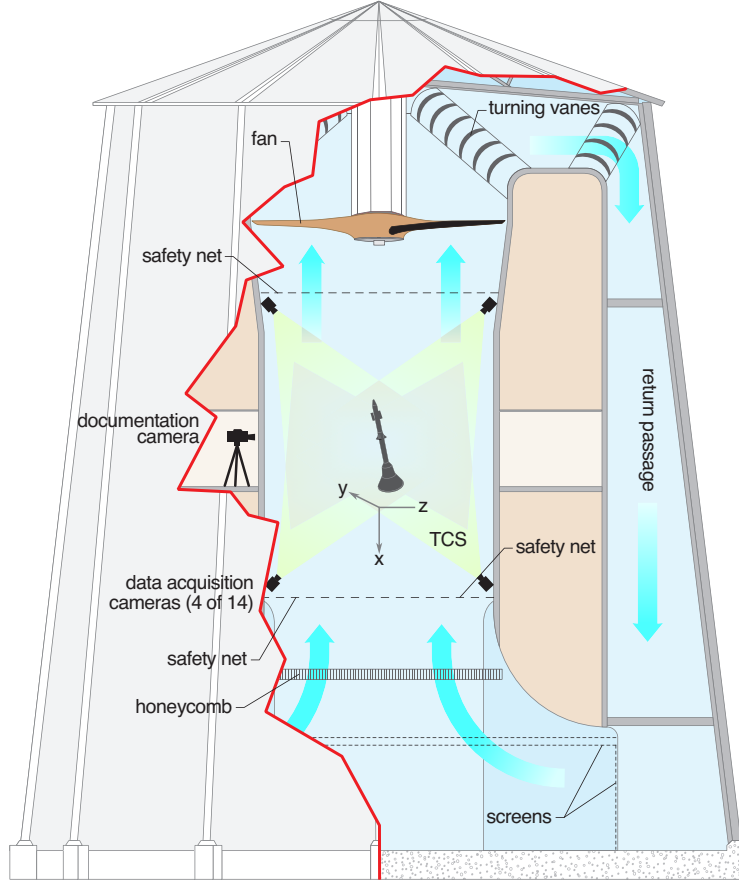
Figure 2. Cross-sectional diagram of the 20-ft Vertical Spin Tunnel.

2.2 Test Articles

Two different model configurations were flown inside the VST during this experiment. The first configuration has the canards on the LAV (see Figure 1) in a stowed state. The second configuration has the canards deployed.

Table 1 provides a summary of the model properties used for this analysis. The test models used in the investigation are 1/29-th dynamically scaled representations of the current LAV design at the time of the experiment. The dynamic scaling was performed using the method outlined by Wolowicz, Bowman, and Gilbert [17] for free flight test articles in the incompressible flow regime. Target values for the test vehicles mass, Moments of Inertia (MOI), and Products of Inertia (POI) are set based on scaling the full size LAV. The test vehicles are ballasted to within $\pm 2\%$ of the target values.

Figure 3 describes the test article's Body Coordinate System (BCS) (X_B, Y_B, Z_B) with the Center

Table 1. Summary of physical properties for the test models.

Property	Value
L, m	0.173
S, m^2	0.0236
m, kg	0.6187
I_{xx}, kg-m^2	0.00100
I_{yy}, kg-m^2	0.01488
I_{zz}, kg-m^2	0.01471
I_{xy}, kg-m^2	0.00009
I_{yz}, kg-m^2	0
I_{xz}, kg-m^2	-0.00018

of Mass (CM) at the origin. The moment coefficients (C_l, C_m, C_n) described in Figure 3 are standard. For this analysis, the aerodynamc force acting on the LAV is described by the force coefficients based on the LAVcoordinate system (C_X, C_Y, C_Z). This system was chosen for its simplicity regarding the data reduction process. α describes the angle of attack. β is the side-slip angle.

Figure 3. Body Coordinate System for the Launch Abort Vehicle.

2.3   Data Acquisition System

The Data Acquisition System (DAS) for this experiment consisted of three parts. The first part is a customized commercially available motion capture system for tracking the test article. The second part is a pitot-static system measuring the dynamic pressure in the wind tunnel. The third part is a commercial video camera for visual recording of the test. The data presented in this report comes from the motion capture and pitot-static systems.
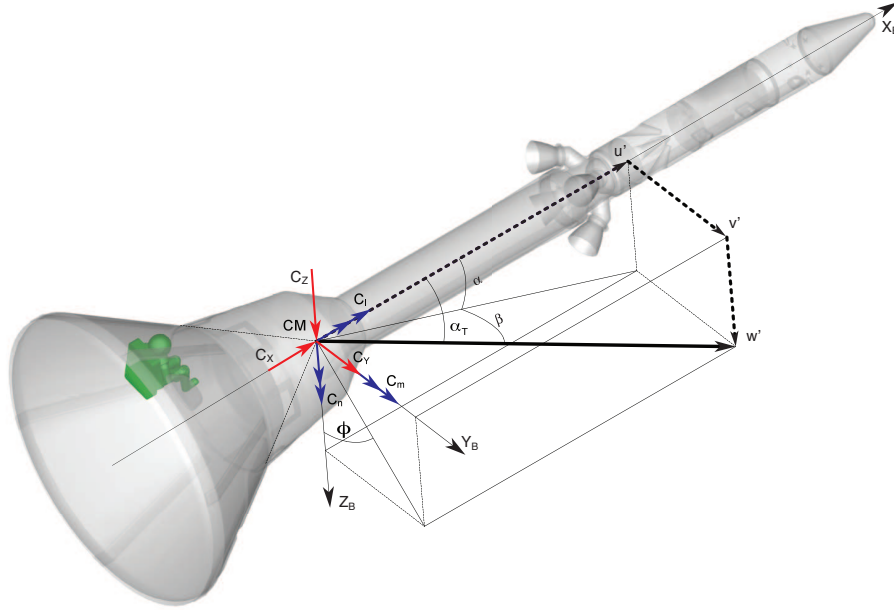
The motion capture system utilizes an array of 8 cameras to capture images of the test section from different vantage points. Small reflective targets, Figure 4 [18], on the model are used as reference targets for the DAS to compare image frames. Using photogrammetry [19, 20], the position and orientation of the model relative to the TCS is obtained. A more detailed description of photogrammetry can be found in Reference [20, www.geodetic.com].

The frame rate of the motion capture in these experiments is 150 Hz. The data returned by the system are the CM position (X, Y, Z) and Euler angles (ϕ, θ, ψ). The Euler angles correspond to a X-Y-Z rotation sequence to map TCS measurements to the BCS.
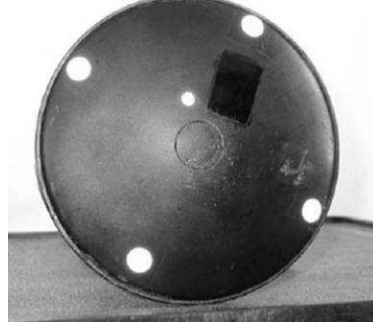
Figure 4. Reflective targets used to capture model motion.

A pitot-static tube measures dynamic pressure ($\bar{q}$) in the wind tunnel. The VST is atmospheric and operates in the subsonic incompressible flow regime. A barometer and thermometer located at the VST are used to measure ambient air pressure and temperature so that air density may be calculated. The air density is assumed to be constant through the VST during the testing. The tunnel airspeed (V) is calculate using the measured dynamic pressure and calculated air density.

It should be noted that the motion capture system has been recently updated using equipment developed by Vicon®. A rigorous error analysis has not been conducted on the system. An informal check regarding the precision of the system is in Reference [18]. The results obtained from this check can be seen in Table 2. There was no attempt to quantify the uncertainty of the wind tunnel velocity and dynamic pressure measurements.

Table 2. Precision of data measured by the Vicon® data acquisition system.

Measurment	σ
ϕ, rad	0.0002
θ, rad	0.0002
ψ, rad	0.0003
X, m	0.0001
Y, m	0.0001
Z, m	0.0001

3 Analysis Method

This section discusses the approach used to model the aerodynamic forces and moments acting on the LAV. Section 3.1 describes the data reduction process for obtaining useful aerodynamics information from experiment observations. Section 3.2 discusses the methods used to obtain the model structures and parameter estimates for the aerodynamic forces and moments.

3.1 Data Reduction

SIDPAC was designed for aircraft which could be fully instrumented with sensors (rate gyros, accelerometers, etc) to collect data. However, the data collected for this investigation was limited to data concerning the model's CM position (X, Y, Z), orientation (Euler angles ϕ, θ, ψ), dynamic pressure $(\bar{q})$, and airspeed(V) inside the VST. The first task of this analysis is to extract the aerodynamic state, forces, and moments. Figure 5 outlines the process used to extract this information from the experiment observations. Subsections 3.1.1 though 3.1.7 details the methods used to obtain the information described in Figure 5.
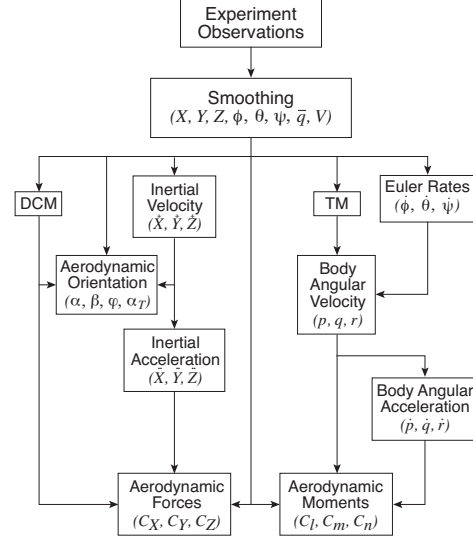
Figure 5. Schematic of data reduction process used to extract aerodynamic information from the experiment observations.

3.1.1 Data Smoothing

Data smoothing removes low power high frequency content from the data. The high frequency content usually contains either noise or higher-order structural responses which are outside the focus of this research. Smoothing data prior to differentiation prevents large increases in noise [21].

The smoothing scheme used for this research uses Fourier analysis to treat the smoothing problem in a global sense. This method is outlined by Morelli and Klein in Reference [22, Section 11.2.3 *Global Smoothing in the Frequency Domain*]. This method requires the analyst to select cut-off frequencies to smooth the signals. These cut-off frequencies need to be large enough to capture the low frequency dynamics and small enough so that high frequency noise is removed. The cut-off frequencies used in this analysis were placed where the frequency content began to decrease towards zero. Figure 6 indicates where cut-off frequencies are chosen relative to the frequency content observed in the VST data. The SIDPAC algorithm, "smoo" [5, 22] is used to implement this smoothing technique.
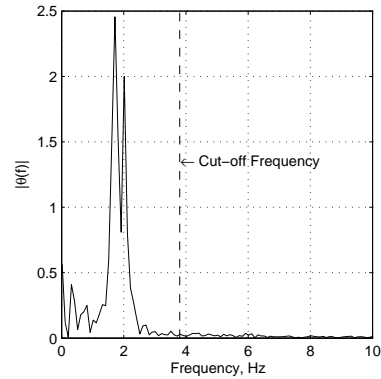
Figure 6. Cut-off frequency selection for smoothing.

6

3.1.2 Transformation Matrices

Two transformation matrices are required for analyzing the data. One transformation matrix is the Direction Cosine Matrix (DCM), $[C]$, to transform vectors from the TCS, see Figure 2 on page 3, to the BCS, see Figure 3 on page 4. The kinematic transformation matrix, $[T]$, is used to transform the Euler rates into the angular velocity vector in the body frame.

The DCM is constructed using the Euler angles for the X-Y-Z rotation sequence [23–26]. The first rotation is for roll, ϕ. The second rotation is pitch, θ. The third rotation is yaw, ψ. Eq. 1 (c is for cosine, s is for sine) yields the DCM that transforms data from TCS to BCS at each point in time.

$$[C] = \begin{bmatrix} c\theta c\psi & c\psi s\theta s\phi + s\psi c\phi & -c\psi s\theta c\phi + s\psi s\phi \\ -c\theta s\psi & -s\psi s\theta s\phi + c\psi c\phi & s\psi s\theta c\phi + c\psi s\phi \\ s\theta & -c\theta s\phi & c\theta c\phi \end{bmatrix} \tag{1}$$

$[T]$ is required to transform the Euler angle rates into body angular rates. Eq. 2 is derived from the X-Y-Z DCM rotation sequence.

$$[T] = \begin{bmatrix} \cos\theta\cos\psi & \sin\psi & 0 \\ -\cos\theta\sin\psi & \cos\psi & 0 \\ \sin\theta & 0 & 1 \end{bmatrix} \tag{2}$$

3.1.3 Inertial and Body Velocities

The inertial velocity vector is calculated by differentiating the position data with respect to time. A five point running 2nd order polynomial performs this differentiation. This method calculates the derivative at each time step using the current data point and its 4 closest neighbors. The four closest neighbors includes two past and two future data points for the majority of the data. The 4 neighboring points become one-sided (either all past or all future data points) as the end points of the data stream are approached. Data close to the endpoints are typically left out of the analysis. A more detailed description of this method can be found in Reference [22, Section 11.4 *Numerical Differentiation*].

Once the inertial velocity is determined, the body velocity can be calculated using the DCM matrix for each data point. Eq. 3 describes the transformation. Angular velocity does not appear in this transform because the CM is collocated with the BCS origin (refer to Figure 3 on page 4).

$$\begin{bmatrix} u \\ v \\ w \end{bmatrix} = [C] \begin{bmatrix} \dot{X} \\ \dot{Y} \\ \dot{Z} \end{bmatrix} \tag{3}$$

3.1.4 Euler and Body Angular Rates

The Euler angles are differentiated using the running polynomial discussed in Section 3.1.3 to determine the Euler rates ($\dot{\phi}$, $\dot{\theta}$, $\dot{\psi}$). Eq. 4 transforms the Euler rates into body angular velocity components.

$$\begin{bmatrix} p \\ q \\ r \end{bmatrix} = [T] \begin{bmatrix} \dot{\phi} \\ \dot{\theta} \\ \dot{\psi} \end{bmatrix} \tag{4}$$

7

3.1.5   Aerodynamic Orientation

The aerodynamic orientation describes the direction of the relative wind vector. The relative wind vector (u',v',w') (See Eq. 5) is a combination of the vehicle's velocity (u, v, w) and the tunnel's free stream vector in the BCS. The tunnel's free stream is assumed to be acting uniformly in the TCS negative x-direction with magnitude V (refer to Figure 2 on page 3).

$$\begin{bmatrix} u' \\ v' \\ w' \end{bmatrix} = \underbrace{\begin{bmatrix} u \\ v \\ w \end{bmatrix}}_{\text{Vehicle}} - \underbrace{[C] \begin{bmatrix} -V \\ 0 \\ 0 \end{bmatrix}}_{\text{Tunnel}} \tag{5}$$

The vehicle's velocity is small in comparison to the wind tunnel free stream vector and can be neglected. The calculation for the relative wind vector components are simplified to Eq. 6.

$$u' = V \cos\theta \cos\psi \tag{6a}$$

$$v' = -V \cos\theta \sin\psi \tag{6b}$$

$$w' = V \sin\theta \tag{6c}$$

The relative wind vector's orientation is typically given in terms of incidence angles. Angle of attack and sideslip angle are typically used for this purpose. The angle of attack and sideslip angle can be calculated directly using Eqs. 7 and 8.

$$\tan\alpha = \frac{w'}{u'} \tag{7}$$

$$\sin\beta = \frac{v'}{V} \tag{8}$$

Total angle of attack and the aerodynamic clock angle are a different set of incidence angles which describe the relative wind vector's orientation. The total angle of attack, α_T, is the angle between the relative wind vector and the body x-axis component of the wind vector (Eq. 9). The aerodynamic clock angle, ϕ_A, is the angle between the body y-axis and z-axis components of the relative wind vector (Eq. 10).

$$\cos\alpha_T = \frac{u'}{V} \tag{9}$$

$$\tan\phi_A = \frac{v'}{w'} \tag{10}$$

NOTE: Most arctangent algorithms provide solutions between $-\pi/2$ and $\pi/2$ (Cartesian quadrants 1 and 4) because they cannot distinguish quadrants 2 and 3. It is important to use component based arctangent algorithms to overcome this deficiency. This research uses an algorithm that provides solutions between 0 and 2π for angle of attack. A different algorithm provides solutions between $-\pi$ and π for the aerodynamic clock angle.

3.1.6   Inertial Accelerations and Aerodynamic Forces

The inertial acceleration of the test article $(\ddot{X},\ \ddot{Y},\ \ddot{Z})$ are obtained by taking the time derivative of the inertial velocity. The time derivatives were taken using the same method described earlier for the inertial velocity. This information can then be used to determine the aerodynamic forces acting on the body. The aerodynamic forces acting on the model are calculated using the Eq. 11 (c is for cosine, s is for sine). For this research the forces are presented in terms of the coefficients $(C_X,\ C_Y,\ C_Z)$ acting along the BCS axes (refer to Figure 3 on page 4).

$$C_X = \frac{m}{\bar{q}S}\left[\left(\ddot{X}-g\right)c\theta c\psi + \ddot{Y}\left(c\psi s\theta s\phi + s\psi c\phi\right) + \ddot{Z}\left(-c\psi s\theta c\phi + s\psi s\phi\right)\right] \tag{11a}$$

$$C_Y = \frac{m}{\bar{q}S}\left[-\left(\ddot{X}-g\right)c\theta s\psi + \ddot{Y}\left(-s\psi s\theta s\phi + c\psi c\phi\right) + \ddot{Z}\left(s\psi s\theta c\phi + c\psi s\phi\right)\right] \tag{11b}$$

$$C_Z = \frac{m}{\bar{q}S}\left[\left(\ddot{X}-g\right)s\theta - \ddot{Y}c\theta s\phi + \ddot{Z}c\theta c\phi\right] \tag{11c}$$

3.1.7   Body Angular Acceleration and Aerodynamic Moments

The body angular accelerations are obtained by differentiating the body angular velocities using the method presented in Section 3.1.3. Euler's equations of motion for rigid bodies can now be applied to the model. These equations describe the net moment acting on the body in the BCS. The moments can be calculated using the body angular rates and accelerations. Eq. 12 displays Euler's equations in terms of the aerodynamic moment coefficients $(C_l,\ C_m,\ C_n)$ acting on the model.

$$C_l = \frac{1}{\bar{q}SL}\left[I_{xx}\dot{p} - I_{xy}\dot{q} - I_{xz}\dot{r} + qr(I_{zz}-I_{yy}) + I_{yz}(r^2-q^2) + I_{xy}pr - I_{xz}qp\right] \tag{12a}$$

$$C_m = \frac{1}{\bar{q}SL}\left[I_{yy}\dot{q} - I_{xy}\dot{p} - I_{yz}\dot{r} + pr(I_{xx}-I_{zz}) + I_{xz}(p^2-r^2) + I_{yz}qp - I_{xy}qr\right] \tag{12b}$$

$$C_n = \frac{1}{\bar{q}SL}\left[I_{zz}\dot{r} - I_{xz}\dot{p} - I_{yz}\dot{q} + qp(I_{yy}-I_{xx}) + I_{xy}(q^2-p^2) + I_{xz}qr - I_{yz}pr\right] \tag{12c}$$

3.2   Data Analysis

This section discusses the tools used to analyze the data and determine models for the aerodynamic forces and moments. Stepwise regression is performed in both the time and frequency domains to determine the model structure for the forces and moments. The method of least squares is used to determine parameter estimates and uncertainties for the force and moment models for each test case. Mean models for each force and moment are developed using covariance weighted averages of the parameter estimates and covariances found for individual test flights.

Sections 3.2.1 through 3.2.4 discusses how these tools are used in more detail. Section 3.2.1 describes the least square method and implementation. Section 3.2.2 describes the tools used to transform the variable time histories in to the frequency domain. Section 3.2.3 describes the stepwise regression process and how it is implemented in this research. Section 3.2.4 describes the covariance weighted mean.

3.2.1 Ordinary Least Squares

Ordinary least squares analysis is the method used to obtain parameter estimates and uncertainties. The stepwise regression uses the least squares model shown in Eq. 13. $\mathbf{H}$ is a matrix of regressors and $\mathbf{x}$ is a vector of unknown parameters. ν is the error between the model and measurements. Eq. 14 describes the estimate of $\mathbf{x}$ using the observations and regressors matrix. $\mathbf{H}^*$ is the conjugate transpose of $\mathbf{H}$.

$$\mathbf{z} = \mathbf{H}\mathbf{x} + \nu \tag{13}$$

$$\mathbf{x} = [\mathrm{Re}\,(\mathbf{H}^*\mathbf{H})]^{-1}\,\mathrm{Re}\,(\mathbf{H}^*\mathbf{z}) \tag{14}$$

Ordinary least squares provides a covariance matrix on the estimates. This covariance can be used to determine the variance on the individual parameters and the correlation between the parameters. The covariance matrix is determined using Eq. 15.

$$\mathbf{\Gamma}_x = \frac{\nu^*\nu}{N-1}\,[\mathrm{Re}\,(\mathbf{H}^*\mathbf{H})]^{-1} \tag{15}$$

To hasten the analysis process, the full data streams for each dependent variable and regressor are not used. Short segments away from the endpoints are used to analyze the data. During flight tests, model residuals are often correlated with neighboring data points [22]. These correlations have a serious effect on the covariance matrix calculated for parameter estimates. Reference [22, Section 5.2, Generalized Least Squares] provides an in-depth discussion on the post processing needed to correct the data. The SIDPAC algorithm "r_colores.m" [5, 22] is used to compute the parameter estimates and covariance matrix for model parameters. This algorithm account for the frequency content of the residuals as well as providing a least squares fit to the data.

3.2.2 Frequency Domain

Performing the analysis in the frequency domain as well as the time domain is a useful analysis technique. Transforming the dependent variable and regressors into the frequency domain helps validate model parameters. Model parameters need to be consistent between both the time and frequency domains. This is due to the independent nature of each regressor.

The z-transform [22] performs the Fourier transform with improved computational efficiency and arbitrary frequency selection. This method uses interpolation of data points to approximate a function with respect to time. This decouples the available frequencies from the data points. The Discrete Fourier Transform (DFT) is then utilized only on the desired band of frequencies.

This feature is very helpful if the data is oversampled. The data presented in this research is sampled at 150 Hz. The standard DFT would compute the frequency domain coefficients for each frequency up to the Nyquist frequency of 75 Hz. The main signal content presented in the data is typically below 5 Hz (See Figure 6).

3.2.3 Stepwise Regression

Stepwise regression will be applied to the force and moment coefficients obtained from the data reduction discussed previously. Stepwise regression is a method for identifying the model structure of a regression equation using a pool of candidate regressors (also obtained from the data reduction). The model structure represents the number and form of terms in the regression equation. A more thorough discussion of stepwise regression can be found in

10

Reference [22, Section 5.4.2 Stepwise Regression]. The SIDPAC algorithm "swr.m" is used to perform the regression. This algorithm uses the method of least squares to determine parameter estimates for the model.

In this research, pools of candidate regressors were formed for each force and moment coefficient. Models are initially formed with only a constant term. A step is taken when a single regressor is either added or removed from the model. Parameter estimates for each regressor and the covariance matrix of the model are updated after each step. The F-ratio (see Eq. 16) is calculated for each included regressor to measure the regressors' importance. Correlations between model residual and excluded regressors are recomputed.

$$F_0 = \frac{\mathbf{x}_j^2}{\sigma_j^2} \tag{16}$$

Regressors are added to the model beginning with the largest correlation until either all regressors are added or the largest correlation with the remaining excluded regressors is less than 0.01. The F-ratio is then checked to see if model parameters need to be removed from the model. A minimum F-ratio of 20 (5 times the value for 95% confidence) is required for all regressors used in modeling the data for this investigation. Regressors that satisfy the minimum F-ratio can also be excluded depending on how the regressor's F-ratio compares to the F-ratio of other regressors and how much the coefficient of determination (R^2) of the model changes when the regressor is added or removed from the model. Regressors with F-ratios substantially lower than other regressors' F-ratios will not contribute much information to the model and can be neglected. This is seen by tracking how much a model's R^2 changes when a regressor is added or removed. If the change in R^2 is small ($< 2\%$) and F-ratio is small compared to others, then the regressor may be removed without degrading the model. A more complete discussion of the F-ratio and it's uses can be found in Reference [22, Section 5.4.3 Stepwise Regression].

3.2.4 Covariance Weighted Mean

This research works with multiple data segments from different test runs. While the model structure may be similar between test runs, the parameter estimates for each test will slightly vary between test runs. A covariance weighted mean is used to combine the different sets of parameter estimates into a single average set to describe all the test data.

Eqs 17 and 18 [27] describes the mean estimate and its covariance, respectively, for n tests. $\mathbf{x}_i$ and $\mathbf{\Gamma}_i$ represent the parameter estimates and covariance matrix for each test.

$$\hat{\mathbf{x}} = \left(\sum_{i=1}^{n} \mathbf{\Gamma}_i^{-1} \right)^{-1} \left(\sum_{i=1}^{n} \mathbf{\Gamma}_i^{-1} \mathbf{x}_i \right) \tag{17}$$

$$\mathbf{\Gamma}_{\hat{x}} = \left(\sum_{i=1}^{n} \mathbf{\Gamma}_i^{-1} \right)^{-1} \tag{18}$$

Using the covariance matrix as the weighting factor places emphasis on the parameter estimates with low uncertainty. Care must be taken with covariance matrices that have large correlation terms between parameter estimates. Large correlations can move the mean parameter estimates outside of the values provided by the separate estimates.

4   Results and Discussion

This section contains the results of the experiment data analysis. Models were identified for C_m, C_n, C_Y, and C_Z. A detailed discussion of these models can be found in sections 4.1-4.4. A summary of the models and parameter estimates for these force and moment coefficients are provided in Section 4.5.

4.1   Pitch Moment Coefficient

Figure 7 shows a plot of C_m versus α for the LAV in the stowed-canard configuration for tests 1, 2, and 3. Static wind tunnel data obtained by the TDT (Ref. [28]) is compared to the VST data in Figure 7. It must be noted that the TDT data was obtained at a Mach number of 0.2 and Reynold's number of 4.7e+6. The VST data was obtained at Mach 0.06 and Reynold's number of 3.0e+5. An "apples-to-apples" comparison cannot be made between the two datasets. However, the comparison is still useful for spotting trends in the data. The final model for C_m is also shown in Figure 7 for comparison.
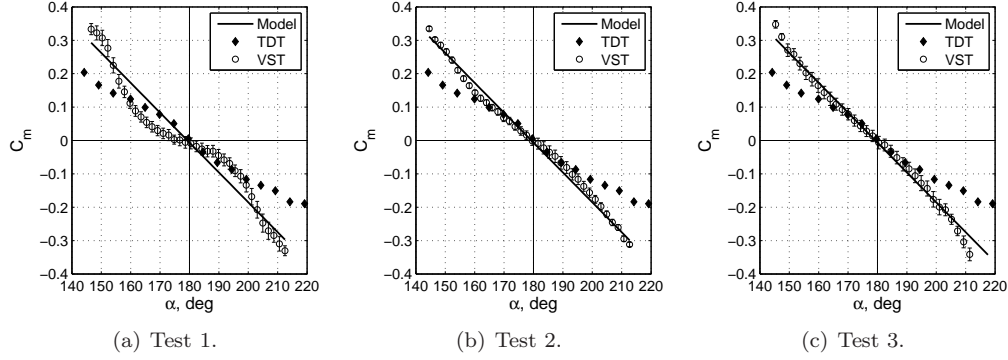

(a) Test 1.   (b) Test 2.   (c) Test 3.

Figure 7. C_m versus α comparison between Vertical Spin Tunnel (VST) data, Transonic Dynamics Tunnel (TDT) data, and the C_m model for the stowed-canard configuration. VST data is at $M = 0.06$ and $Re = 3$e+5. TDT data is at $M = 0.2$ and $Re = 4.7$e+6. Error bars represent 1σ standard deviation.

Figure 7 indicates that the LAV is statically stable in the heat shield-forward flight direction. Figure 7(a) indicates a highly nonlinear relationship between α and C_m for test 1, while Figures 7(b) and 7(c) demonstrate a more linear relationship with some nonlinear trend observed at the extremes of the α range. The VST data and model shown in Figure 7 describe a steeper slope than the TDT data. Figure 7(b) and 7(c) indicate that VST and TDT data are in close agreement at angles of attack near 180 degrees. However, the VST and TDT diverge at angles of attack further away from 180 degrees. The $C_m - \alpha$ slope appear to lessen toward the extremes of the TDT data. The VST data indicate that the $C_m - \alpha$ slope increase near the extremes.

Figure 8 describes the C_m-α behavior for the LAV in the deployed-canard configuration seen in tests 4 and 8. The identified model is displayed with the VST data for comparison. No static wind tunnel data was available for comparison for the deployed-canard configuration. Test 4 in Figure 8(a) shows a slightly cubic relationship between C_m and α. However, the data also appears to lie along the line representing the identified model for the deployed-canard configuration. Figure 8(b) (test 8) demonstrates a more linear relationship between C_m and α which almost falls on the model line exactly with a couple outliers. Figure 8 shows that the zero crossing is shifted from 180 degrees to about 174 degrees angle of attack.
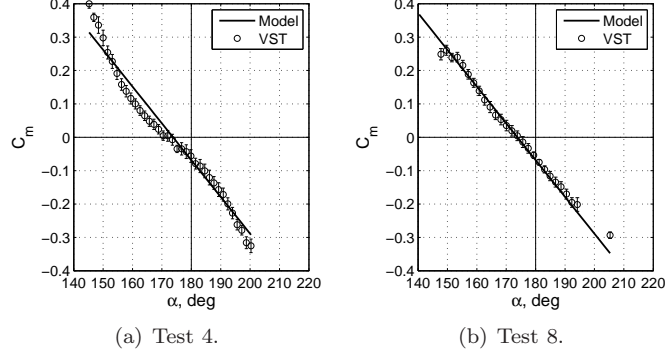
12

(a) Test 4. (b) Test 8.

Figure 8. C_m vs α comparison between Vertical Spin Tunnel (VST) data and the C_m model for the deployed-canard configuration. Vertical Spin Tunnel (VST) data is at $M = 0.06$ and $Re = 3\text{e}+5$. Error bars represent 1σ standard deviation.

Table 3. C_m model structures identified using stepwise regression.

Tests	Time Domain	Frequency Domain
1^a	$C_{m_0} + C_{m_{\alpha'}}(\alpha - \pi) + C_{m_{\alpha'3}}(\alpha - \pi)^3$	$C_{m_{\alpha'}}(\alpha - \pi)$
2^a	$C_{m_0} + C_{m_{\alpha'}}(\alpha - \pi)$	$C_{m_{\alpha'}}(\alpha - \pi)$
3^a	$C_{m_0} + C_{m_{\alpha'}}(\alpha - \pi)$	$C_{m_{\alpha'}}(\alpha - \pi)$
4^b	$C_{m_0} + C_{m_{\alpha'}}(\alpha - \pi) + C_{m_{\alpha'3}}(\alpha - \pi)^3$	$C_{m_{\alpha'}}(\alpha - \pi) + C_{m_p}\frac{pL}{2V}$
8^b	$C_{m_0} + C_{m_{\alpha'}}(\alpha - \pi)$	$C_{m_{\alpha'}}(\alpha - \pi) + C_{m_p}\frac{pL}{2V}$

[a] Stowed-canard configuration.
[b] Deployed-canard configuration.

Table 4. Parameter estimates for C_m.

Tests	Time Domain		Frequency Domain
	C_{m_0} (σ)	$C_{m_{\alpha'}}$ (σ)	$C_{m_{\alpha'}}$ (σ)
1^a	-0.007 (0.002)	-0.50 (0.01)	-0.51 (0.01)
2^a	-0.005 (0.002)	-0.50 (0.01)	-0.497 (0.008)
3^a	-0.010 (0.004)	-0.53 (0.01)	-0.53 (0.02)
Mean^a	-0.006 (0.001)	-0.513 (0.007)	-0.505 (0.006)
4^b	-0.076 (0.003)	-0.67 (0.01)	-0.67 $(0.01)^c$
8^b	-0.063 (0.003)	-0.615 (0.009)	-0.62 $(0.02)^c$
Mean^b	-0.069 (0.002)	-0.631 (0.008)	-0.65 (0.01)

[a] Stowed-canards configuration.
[b] Deployed-canards configuration.
[c] Frequency domain estimate adjusted for bias.

Table 3 provides a summary of the model structures identified by the stepwise regression in the time and frequency domains. All of the identified models feature a $C_{m_{\alpha'}}$ term for both configurations. $C_{m_{\alpha'}}$ represents the slope of $C_m - \alpha$ near the angle of attack at 180 degrees (π radians). A regressor of $(\alpha - \pi)$ was chosen to represent the data since the angle of attack data stayed close to 180 degrees. Only the regressions of tests 1 and 4 in the time domain indicate that the cubic angle of attack term is significant for the canard-stowed and deployed-canard configurations,respectively. This makes sense given the cubic relationship between $C_m - \alpha$ seen in Figures 7(a) and 8(a), respectively. This cubic term may be representative of wind tunnel effects that are not captured by the data. These unobserved effects may be responsible for why test 1 remained in the same Y-Z location for the duration of its flight unlike tests 2 and 3 which moved about the VST.

Table 3 shows that the stepwise regression indicates that the body angular roll rate (p) is significant to the deployed-canard configuration model in the frequency domain. This is due to the increased constant term (C_{m_0}) when the canards are deployed. This was proven by calculating $C_m - C_{m_0}$ in the frequency domain and redoing the stepwise regression for tests 4 and 8. Removing the constant term in the time domain decreased the importance of p in the frequency domain. The final model for C_m is shown in Equation 19. The terms shown in Equation 19 are consistent throughout the tests. Equation 19 is simple and accounts for most of the data obtained through the tests.

$$C_m = C_{m_0} + C_{m_{\alpha'}} (\alpha - \pi) \tag{19}$$

The stepwise regression reveals Equation 19 to be the common model between all tests described in Table 3 for both stowed-canard and deployed-canard configurations. Table 4 shows the parameter estimates and the covariance weighted mean estimates for the two configurations in the time and frequency domains. Figure 18 provides a graphical comparison of the parameter estimates described in Table 4. Figure 9 shows that both time and frequency domain estimates for $C_{m_{\alpha'}}$ are nearly identical. The estimates for C_{m_0} and $C_{m_{\alpha'}}$ do not significantly change between test runs which indicates an accurate model structure was identified.
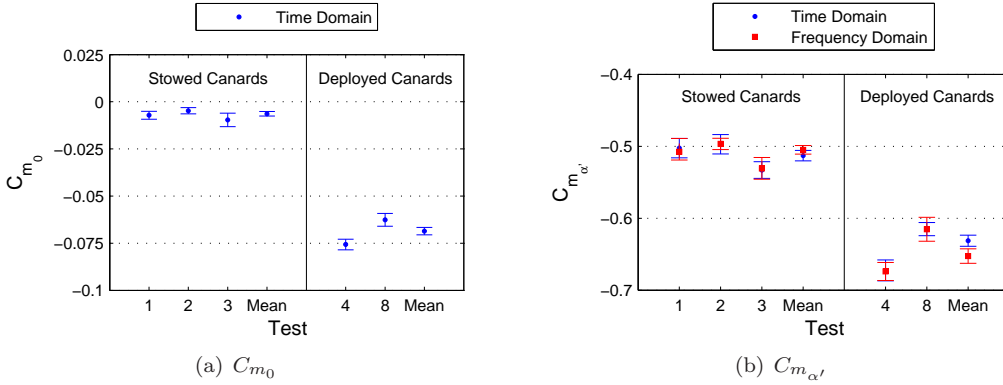

(a) C_{m_0}

(b) $C_{m_{\alpha'}}$

Figure 9. Comparison of pitch moment coefficient model parameters. Error bars represent 1σ standard deviation.

4.2   Yaw Moment Coefficient

Figure 10 shows a plot of C_n versus β for the stowed-canard configuration for tests 1, 2, and 3. Figure 10 compares the VST data to the identified C_n model. Figure 10 indicates that the LAV is statically stable in the heat shield-forward flight direction. Figure 10(a) shows a very linear relationship between β and C_n for test 1 that falls almost exactly on the model line. Figures 10(b) and 10(c) indicate a slightly nonlinear relationship between C_n and β for tests 2 and 3. The linear C_n model still appears to accurately reflect the VST data captured during testing.
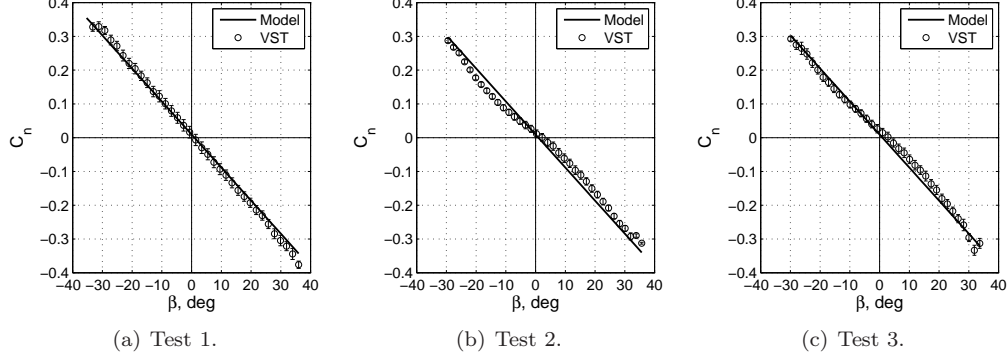

| (a) Test 1. | (b) Test 2. | (c) Test 3. |

Figure 10. C_n versus β comparison between Vertical Spin Tunnel (VST) data and the C_n model for the stowed-canard configuration. VST data is at $M = 0.06$ and $Re = 3\mathrm{e}{+}5$. Error bars represent 1σ standard deviation.

Figure 11 describes the C_n-β behavior for the deployed-canard configuration seen in tests 4 and 8. The identified model is displayed with the VST data for comparison. No static wind tunnel data was available for comparison for the deployed-canard configuration. Figure 10 shows that both tests show a linear between C_n and β which is captured by the identified model. However, the data also appears to lie along the identified model for the deployed-canard configuration.
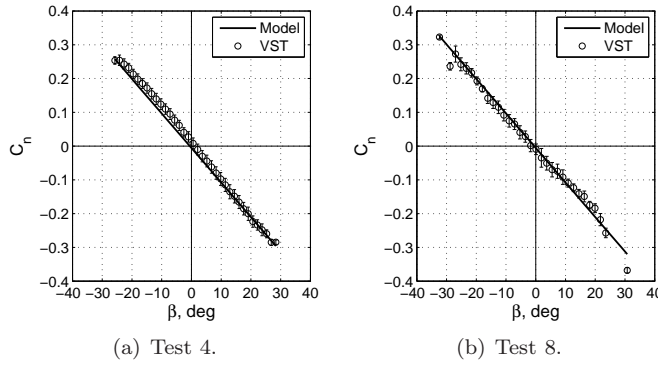

| (a) Test 4. | (b) Test 8. |

Figure 11. C_n versus β comparison between Vertical Spin Tunnel (VST) data and the C_n model for the deployed-canard configuration. VST data is at $M = 0.06$ and $Re = 3\mathrm{e}{+}5$. Error bars represent 1σ standard deviation.

Table 5 provides a summary of the model structures identified using stepwise regression in the time and frequency domains. The time and frequency domain model structures consistently describe a linear model (Equation 20). C_{n_0} is the constant bias term and only appears

15

Table 5. C_n model structures identified using stepwise regression.

Tests	Time Domain	Frequency Domain
1^a	$C_{n_0} + C_{n_\beta}\beta$	$C_{n_\beta}\beta$
2^a	$C_{n_0} + C_{n_\beta}\beta$	$C_{n_\beta}\beta$
3^a	$C_{n_0} + C_{n_\beta}\beta$	$C_{n_\beta}\beta$
4^b	$C_{n_0} + C_{n_\beta}\beta$	$C_{n_\beta}\beta$
8^b	$C_{n_0} + C_{n_\beta}\beta$	$C_{n_\beta}\beta$

[a]Stowed-canard configuration.
[b]Deployed-canard configuration.

in the time domain. Table 6 describes the least squares parameter estimates and covariance weighted mean estimates for both stowed-canard and deployed-canard configurations.

$$C_n = C_{n_0} + C_{n_\beta}\beta \tag{20}$$

Figure 12 provides a graphical comparison of the parameter estimates for C_{n_0} and C_{n_β}. The time domain estimates for C_{n_0} have nearly the same value for all the stowed canard test runs. C_{n_0} appears to significantly change between test runs for the deployed canard configuration. The reason the deployed canard mean value is closer to the test 8 is because of the smaller uncertainty and a significant correlation between C_{n_β} and C_{n_0} which would drive the covariance weighted mean toward the test 8 estimate. This same phenomena can be seen in C_{n_β} for the stowed canard test runs.

Table 6. Parameter estimates for C_n.

Tests	Time Domain		Frequency Domain
	C_{n_0} (σ)	C_{n_β} (σ)	C_{n_β} (σ)
1^a	0.008 (0.002)	-0.59 (0.01)	-0.59 (0.01)
2^a	0.009 (0.001)	-0.51 (0.02)	-0.507 (0.007)
3^a	0.013 (0.003)	-0.54 (0.01)	-0.54 (0.01)
Mean^a	0.0092 (0.0008)	-0.561 (0.007)	-0.532 (0.005)
4^b	0.008 (0.002)	-0.62 (0.01)	-0.61 (0.02)
8^b	-0.007 (0.001)	-0.56 (0.01)	-0.56 (0.02)
Mean^b	-0.0057 (0.0009)	-0.586 (0.008)	-0.59 (0.01)

[a]Stowed-canard configuration.
[b]Deployed-canard configuration.
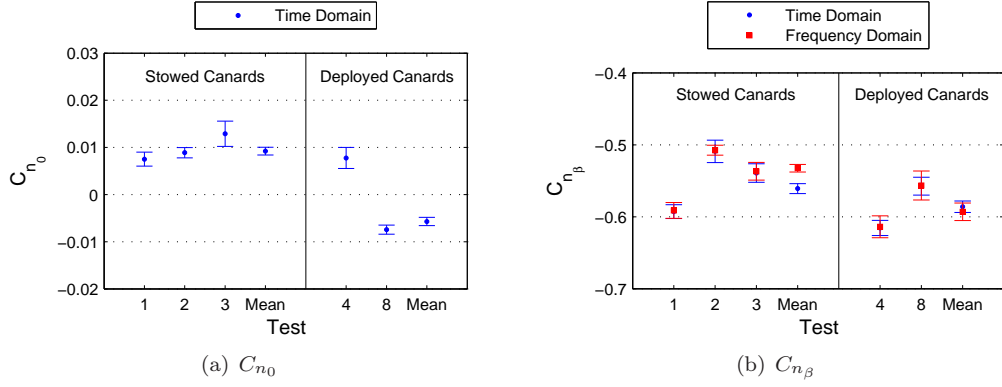
(a) C_{n_0}

(b) C_{n_β}

Figure 12. Comparison of yaw moment coefficient model parameters. Error bars represent 1σ standard deviation.

4.3   Body Y-Force Coefficient

Figure 13 shows a plot of C_Y versus β for the LAV in the stowed-canard configuration for tests 1, 2, and 3. Figure 13 displays the model (Equation 21) for C_Y without the C_{Y_r} term. Static wind tunnel data was not explicitly available for comparison. The VST data is displayed based on the average C_Y for different partitions of side slip angle (β). The error bar represents 1σ uncertainty based on the partition populations.

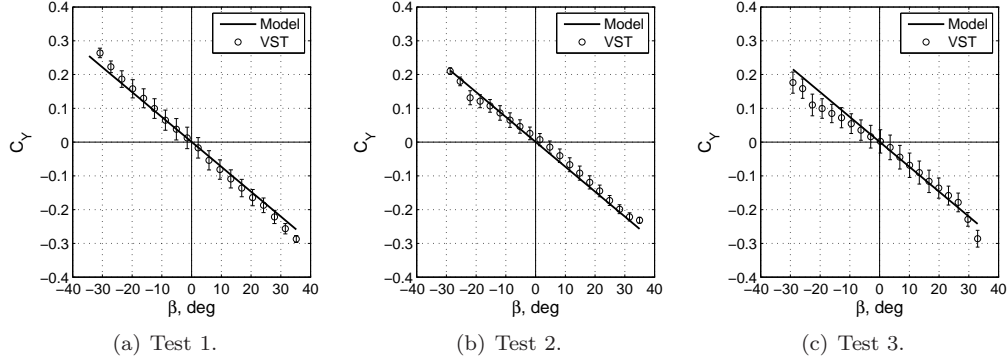(a) Test 1.

(b) Test 2.

(c) Test 3.

Figure 13. C_Y versus β comparison between Vertical Spin Tunnel (VST) data and the C_Y model for the stowed-canard configuration. VST data is at $M = 0.06$ and $Re = 3\text{e}{+}5$. Error bars represent 1σ standard deviation.

Figure 13(a) indicates that C_Y has a very linear relationship with β. Figures 13(b) and 13(c) describe a slightly nonlinear relationship between C_Y and β. The linear model appears to track C_Y very well and start to diverge around the endpoints.

Figure 14 describes the C_Y-β behavior for the LAV in the deployed-canard configuration seen in tests 4 and 8. The model is calculated using Equation 21 without the C_{Y_r} term. Test 4 in Figure 14(a) describes a linear $C_Y - \beta$ relationship for test 4. Test 8 (Figure 14(b)) shows a nonlinear relationship between C_Y and β.

Table 7 provides a summary of the model structures identified by the stepwise regression in the time and frequency domains. Test 3 is the only test in which the stepwise regression yields a model structure that is different from Equation 21. C_{Y_β} accounts for the majority of the frequency content seen in the data. While C_{Y_r} is identified by the stepwise regression,
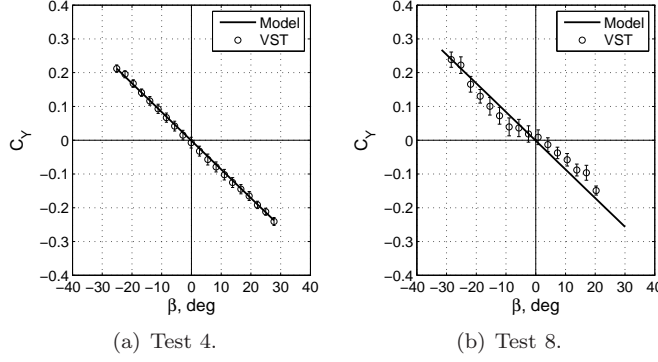
17

(a) Test 4.   (b) Test 8.

Figure 14. C_Y versus β comparison between Vertical Spin Tunnel (VST) data and the C_Y model for the deployed-canard configuration. VST data is at $M = 0.06$ and $Re = 3\mathrm{e}{+}5$. Error bars represent 1σ standard deviation.

it tends to be a much smaller contributer to the model.

Table 7. C_n model structures identified using stepwise regression.

Tests	Time Domain	Frequency Domain
1^a	$C_{Y_0} + C_{Y_\beta}\beta + C_{Y_r}\frac{rL}{2V}$	$C_{Y_\beta}\beta + C_{Y_r}\frac{rL}{2V}$
2^a	$C_{Y_0} + C_{Y_\beta}\beta + C_{Y_r}\frac{rL}{2V}$	$C_{Y_\beta}\beta + C_{Y_r}\frac{rL}{2V}$
3^a	$C_{Y_0} + C_{Y_\beta}\beta + C_{Y_q}\frac{qL}{2V}$	$C_{Y_\beta}\beta + C_{Y_q}\frac{qL}{2V}$
4^b	$C_{Y_0} + C_{Y_\beta}\beta + C_{Y_r}\frac{rL}{2V}$	$C_{Y_\beta}\beta + C_{Y_r}\frac{rL}{2V}$
8^b	$C_{Y_0} + C_{Y_\beta}\beta + C_{Y_r}\frac{rL}{2V}$	$C_{Y_\beta}\beta + C_{Y_r}\frac{rL}{2V}$

[a]Stowed-canard configuration.
[b]Deployed-canard configuration.

Table 8 displays the parameter estimates and the covariance weighted mean estimates for the two configurations in the time and frequency domains. The values are the results of the ordinary least squares method described in Section 3.2.1. Notice that the frequency domain values for C_{Y_r} are not as consistent as the time domain values. This may indicate that only C_{Y_β} is necessary for an adequate model.

$$C_Y = C_{Y_0} + C_{Y_\beta}\beta + C_{Y_r}\frac{rL}{2V} \tag{21}$$

Table 8 indicates that the canards have a minor affect on C_Y. C_{Y_β} and C_{Y_r} appear to change only slightly based on the mean estimates. There is a slight increase in the magnitude of C_{Y_β}, and a small decrease in the magnitude of C_{Y_r}.

Figure 15 displays a graphical comparison of the model parameters in Table 8 for each test and mean combination for the stowed and deployed canard configurations. Figure 15(a) indicates that C_{y_0} may be sensitive to the test run, with the estimate for test 3 being significantly different from the other tests. Figures 15(b) and 15(c) display frequency domain estimates with large uncertainties on parameters C_{Y_β} and C_{Y_r} for test 3. This may signal that the identified model may not be sufficient for test 3 and that some information was not

Table 8. Parameter estimates for C_Y.

Tests	Time Domain			Frequency Domain	
	C_{Y_0} (σ)	C_{Y_β} (σ)	C_{Y_r} (σ)	C_{Y_β} (σ)	C_{Y_r} (σ)
1[a]	0.001 (0.003)	-0.468 (0.009)	-2.5 (0.3)	-0.48 (0.08)	-4 (2)
2[a]	0.004 (0.001)	-0.396 (0.008)	-1.9 (0.2)	-0.34 (0.04)	-2 (1)
3[a]	-0.014 (0.003)	-0.38 (0.02)	-2.0 (0.5)	-0.5 (0.1)	-3 (4)
Mean[a]	0.001 (0.001)	-0.422 (0.006)	-2.2 (0.2)	-0.37 (0.03)	-3.5 (0.9)
4[b]	-0.0017 (0.0008)	-0.493 (0.007)	-1.4 (0.2)	-0.50 (0.04)	-2 (1)
8[b]	-0.001 (0.003)	-0.40 (0.03)	-2.0 (0.7)	-0.35 (0.07)	-2 (2)
Mean[b]	-0.0016 (0.0007)	-0.487 (0.007)	-1.5 (0.2)	-0.46 (0.03)	-1.5 (0.9)

[a]Stowed-canard configuration.
[b]Deployed-canard configuration.

captured by the data. The deployed canard configuration estimates remain similar though out the test runs indicating an accurate model was identified.
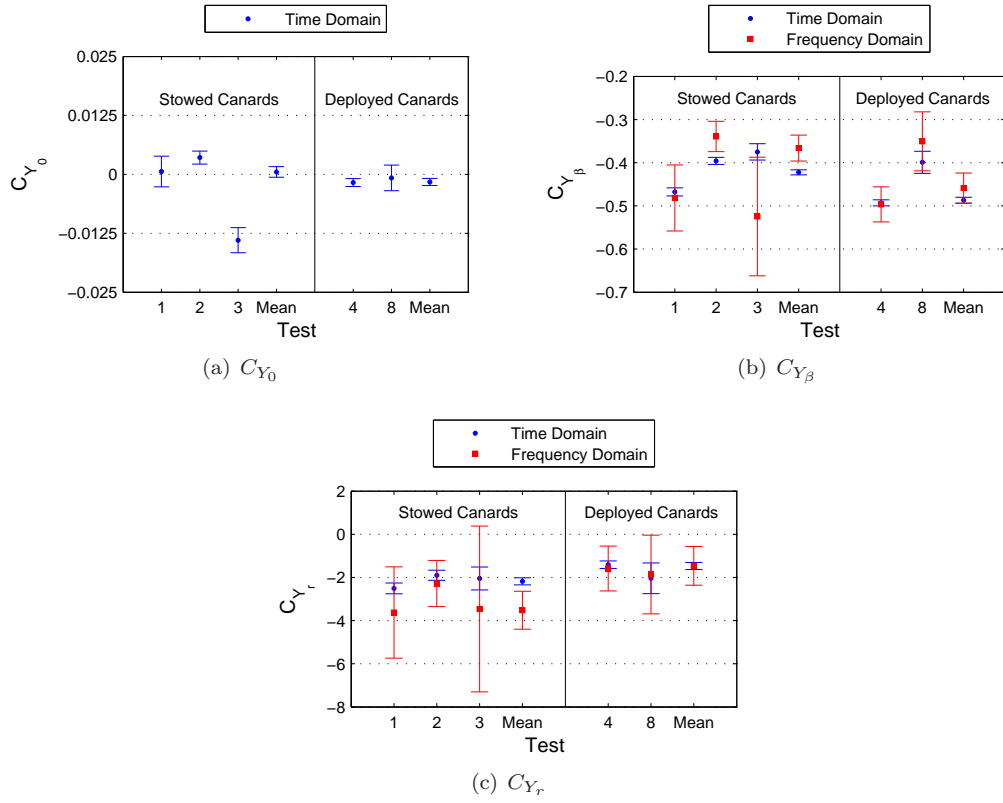
(a) C_{Y_0}

(b) C_{Y_β}

(c) C_{Y_r}

Figure 15. Comparison of Y-force coefficient model parameters. Error bars represent 1σ standard deviation.

4.4 Body Z-Force Coefficient

Figure 16 shows a plot of C_Z versus α for the LAV in the stowed-canard configuration for tests 1, 2, and 3. Static wind tunnel data obtained by the TDT is compared to the VST data in Figure 16. The identified model is also plotted alongside the TDT and VST data for comparison. The TDT data was obtained at a Mach number of 0.2 and Reynold's number of 4.7e+6. The VST data was obtained at Mach 0.06 and Reynold's number of 3.0e+5. The model uses only C_{Z_0} and $C_{Z_{\alpha'}}$ terms.

(a) Test 1. (b) Test 2. (c) Test 3.
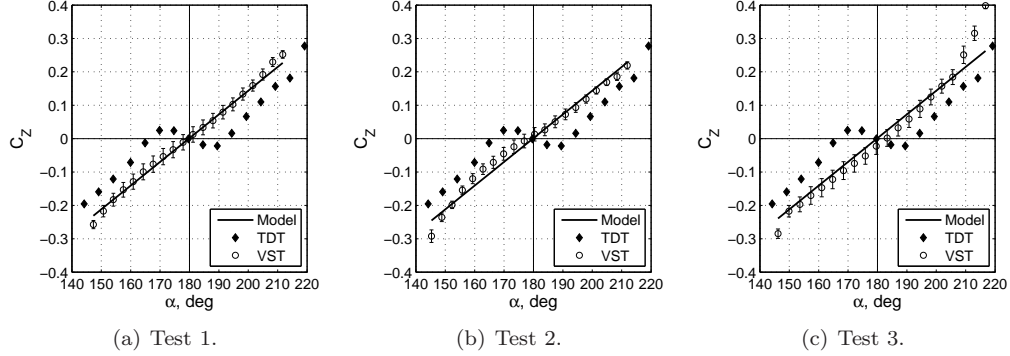
Figure 16. C_Z versus α comparison between Vertical Spin Tunnel (VST) data, Transonic Dynamics Tunnel (TDT) data, and the C_Z model for the stowed-canard configuration. VST data is at $M = 0.06$ and $Re = 3$e+5. TDT data is at $M = 0.2$ and $Re = 4.7$e+6. Error bars represent 1σ standard deviation.

Figure 16 showes that the TDT and VST present different $C_Z - \alpha$ behaviors at angles of attack close to 180 degrees. The TDT data presents a highly nonlinear relationship compared to the VST data. This difference is most likely due to the difference in Reynolds numbers. It is interesting to note that the slope of the C_Z versus α for the TDT data becomes similar to the slope represented by the VST data at angles of attack farther away from 180 degrees.
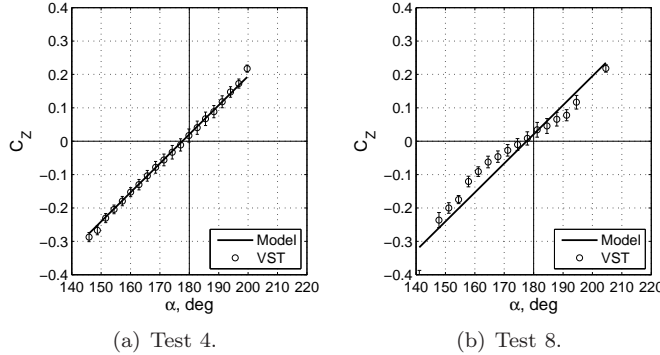

(a) Test 4. (b) Test 8.

Figure 17. C_Z versus α comparison between Vertical Spin Tunnel (VST) data and the C_Z model for the deployed-canard configuration. VST data is at $M = 0.06$ and $Re = 3$e+5. Error bars represent 1σ standard deviation.

Figure 17 describes the C_Z-α behavior for the LAV in the deployed-canard configuration seen in tests 4 and 8. The identified model displayed with the VST data for comparison. No static wind tunnel data was available for comparison for the deployed-canard configuration.

Test 8 in Figure 17(b) shows a slightly nonlinear relationship between C_Z and α. Figure 17 shows that the zero crossing is shifted from 180 degrees to about 177 degrees angle of attack.

Table 9 provides a summary of the model structures identified by the stepwise regression in the time and frequency domains. All of the identified models feature the model (Equation 22) for both configurations. Only test 8 appears to favor an additional nonlinear term ($C_{Z_{\alpha'3}}$). This makes sense given the cubic relationship between $C_Z - \alpha$ seen in Figure 17(b). No other test indicates a strong cubic relationship between C_Z and α.

Table 9. C_Z model structures identified using stepwise regression.

Tests	Time Domain	Frequency Domain
1^a	$C_{Z_0} + C_{Z_{\alpha'}}\left(\alpha - \pi\right) + C_{Z_q}\frac{qL}{2V}$	$C_{Z_{\alpha'}}\left(\alpha - \pi\right) + C_{Z_q}\frac{qL}{2V}$
2^a	$C_{Z_0} + C_{Z_{\alpha'}}\left(\alpha - \pi\right) + C_{Z_q}\frac{qL}{2V}$	$C_{Z_{\alpha'}}\left(\alpha - \pi\right) + C_{Z_q}\frac{qL}{2V}$
3^a	$C_{Z_0} + C_{Z_{\alpha'}}\left(\alpha - \pi\right) + C_{Z_q}\frac{qL}{2V} + C_{Z_r}\frac{rL}{2V}$	$C_{Z_{\alpha'}}\left(\alpha - \pi\right) + C_{Z_q}\frac{qL}{2V} + C_{Z_r}\frac{rL}{2V}$
4^b	$C_{Z_0} + C_{Z_{\alpha'}}\left(\alpha - \pi\right) + C_{Z_q}\frac{qL}{2V}$	$C_{Z_{\alpha'}}\left(\alpha - \pi\right) + C_{Z_p}\frac{pL}{2V} + C_{Z_q}\frac{qL}{2V}$
8^b	$C_{Z_0} + C_{Z_{\alpha'}}\left(\alpha - \pi\right) + C_{Z_{\alpha'3}}\left(\alpha - \pi\right)^3$ $+C_{Z_q}\frac{qL}{2V}$	$C_{Z_{\alpha'}}\left(\alpha - \pi\right) + C_{Z_{\alpha'3}}\left(\alpha - \pi\right)^3$ $+C_{Z_p}\frac{pL}{2V} + C_{Z_q}\frac{qL}{2V}$

[a]Stowed-canard Configuration.
[b]Deployed-canard configuration.

Table 9 shows that the stepwise regression indicates that the body angular roll rate (p) is significant to the deployed-canard configuration model in the frequency domain. This is likely due to the same reasons why p appeared in the frequency domain regression for C_m. Equation 22 also displays a symmetry with Equation 21 which makes sense given the axisymmetric nature of the LAV.

$$C_Z = C_{Z_0} + C_{Z_{\alpha'}}\left(\alpha - \pi\right) + C_{Z_q}\frac{qL}{2V} \tag{22}$$

Table 10 shows the parameter estimates that were obtained using Equation 22 for the model structure. Values are rounded based on the significant figures indicated by their uncertainty (σ). The canards appear to increase the values of the model parameters. C_{Z_0} increases by about 0.02, $C_{Z_{\alpha'}}$ increases by 0.1, and C_{Z_q} increases by about 0.5.

Figure 18 displays a graphical comparison of the model parameters in Table 10 for each test and mean combination for the stowed and deployed canard configurations. Figure 18(a) shows consistent estimates for C_{Z_0} for both the stowed and deployed canard test runs. Figure 18(b) shows similar consistent time and frequency domain for test runs with the exception of test 3. Test 3 provided a much lower estimate for $C_{Z_{\alpha'}}$ with larger uncertainty. Figure 18(c) shows consistent estimates for C_{Z_q} for both stowed and deployed canard configurations. However, the uncertainties on C_{Z_q} for tests 1 and 3 indicate that some information may be missing from either the model structure or test data.

Table 10. Parameter estimates for C_Z.

Tests	Time Domain			Frequency Domain	
	C_{Z_0} (σ)	$C_{Z_{\alpha'}}$ (σ)	C_{Z_q} (σ)	$C_{Z_{\alpha'}}$ (σ)	C_{Z_q} (σ)
1^a	0.005 (0.002)	0.425 (0.008)	1.7 (0.3)	0.43 (0.08)	3 (3)
2^a	0.000 (0.001)	0.392 (0.005)	1.4 (0.2)	0.33 (0.03)	1.1 (0.9)
3^a	-0.003 (0.003)	0.44 (0.01)	0.7 (0.3)	0.2 (0.1)	1 (3)
Mean^a	0.0013 (0.0009)	0.407 (0.004)	1.4 (0.1)	0.36 (0.03)	1.0 (0.8)
4^b	0.022 (0.002)	0.52 (0.01)	1.8 (0.3)	0.52 $(0.02)^c$	2.0 $(0.5)^c$
8^b	0.023 (0.004)	0.41 (0.02)	1.9 (0.6)	0.39 $(0.03)^c$	3 $(1)^c$
Mean^b	0.021 (0.002)	0.499 (0.009)	1.9 (0.3)	0.49 (0.02)	2.5 (0.5)

^{a}Stowed-canard configuration.
^{b}Deployed-canard configuration.
^{c}Frequency domain estimate adjusted for bias.

(a) C_{Z_0}

(b) $C_{Z_{\alpha'}}$

(c) C_{Z_q}
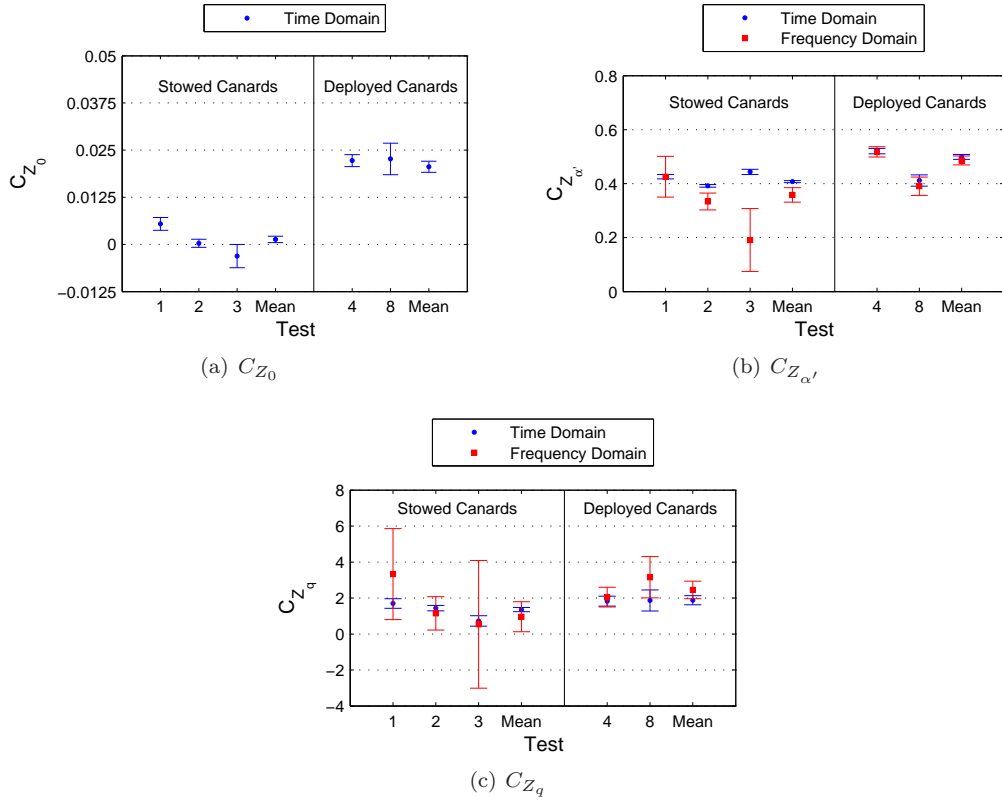
Figure 18. Comparison of Z-force coefficient model parameters. Error bars represent 1σ standard deviation.

4.5 Results Summary

The stepwise regression method described in Section 3.2.3 reveals that linear models can adequately describe the aerodynamic pitch and yaw moment coefficients (Eqs. 19 and 20, respectively), and body Y-force and Z-force coefficients (Eqs. 21 and 22, respectively). Models for the body X-force coefficient, and roll moment coefficient were not obtained.

$$C_m = C_{m_0} + C_{m_{\alpha'}} (\alpha - \pi) \tag{19}$$

$$C_n = C_{n_0} + C_{n_\beta} \beta \tag{20}$$

$$C_Y = C_{Y_0} + C_{Y_\beta} \beta + C_{Y_r} \frac{rL}{2V} \tag{21}$$

$$C_Z = C_{Z_0} + C_{Z_{\alpha'}} (\alpha - \pi) + C_{Z_q} \frac{qL}{2V} \tag{22}$$

Table 11. Parameter estimates obtained for the models for C_m, C_n, C_Y, and C_Z for both stowed-canard and deployed-canard configurations.

	Time Domain		Frequency Domain	
	Stowed	Deployed	Stowed	Deployed
Parameter	$\mathbf{x}(\sigma)$	$\mathbf{x}(\sigma)$	$\mathbf{x}(\sigma)$	$\mathbf{x}(\sigma)$
C_{m_0}	-0.006 (0.001)	-0.069 (0.002)	–	–
$C_{m_{\alpha'}}$	-0.513 (0.007)	-0.631 (0.008)	-0.505 (0.006)	-0.65 (0.01)
C_{n_0}	0.009 (0.001)	-0.006 (0.001)	–	–
C_{n_β}	-0.561 (0.007)	-0.585 (0.008)	-0.532 (0.005)	-0.59 (0.01)
C_{Y_0}	0.001 (0.001)	-0.002 (0.001)	–	–
C_{Y_β}	-0.422 (0.006)	-0.487 (0.007)	-0.46 (0.03)	-0.48 (0.01)
C_{Y_r}	-2.2 (0.2)	-1.5 (0.2)	-3.5 (0.9)	-1.5 (0.9)
C_{Z_0}	0.001 (0.001)	0.021 (0.002)	–	–
$C_{Z_{\alpha'}}$	0.407 (0.004)	0.499 (0.009)	0.36 (0.03)	0.49 (0.02)
C_{Z_q}	1.4 (0.1)	1.9 (0.3)	1.0 (0.8)	2.5 (0.5)

Parameter estimates for Eqs. 19-22 are provided in Table 11. A graphical comparison of these parameters can be found in Figure 19. The estimates and uncertainties are calculated using a covariance weighted average (see Section 3.2.4) of parameter estimates obtained for each test run. The estimates shown in Table 11 are displayed based on the significant digits of the uncertainties. Frequency domain estimates for the constant terms are not shown in Table 11. Large constant terms can bias frequency domain estimates toward low frequency content. This is prevented by removing these biases before transforming data to the frequency domain. The constant terms are not compared in Figure 19.

Figure 19 compares the estimates for parameters determined in both the time and frequency domains. The close agreement between time and frequency domain estimates indicate that the model structures described by Eqs. 19-22 are accurate. Figure 19 also displays the effect that the canards have on the model parameters. Figure 19 and Table 11 show that
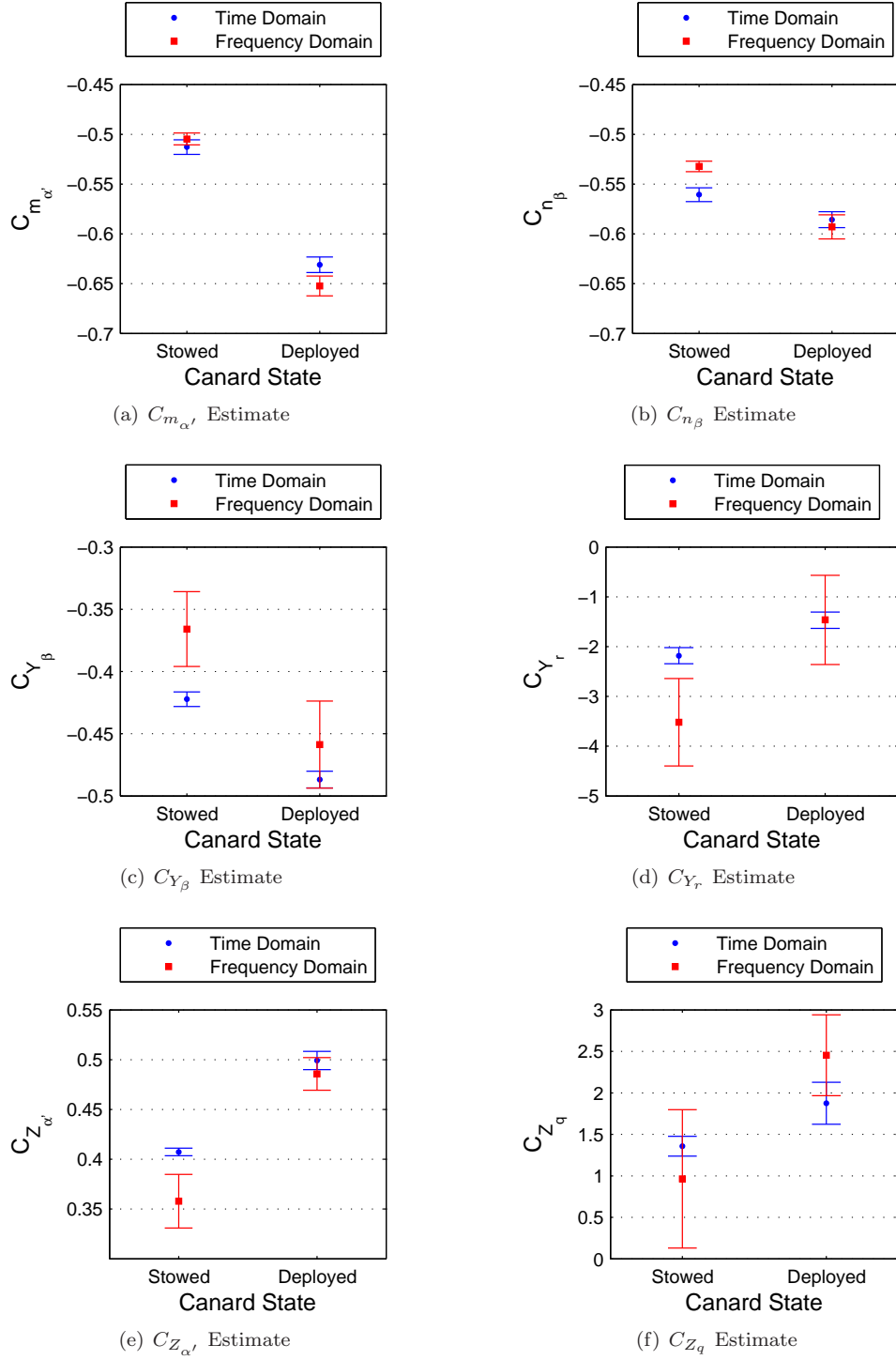
Figure 19. Graphical comparison of model parameter estimates in the time and frequency domains. Error bars represent 1σ standard deviation.

the canards change the magnitude of all model parameters except for the constant terms, C_{n_0} and C_{Y_0}.

Table 12 provides each model's Mean Squared Fit Error (MSFE) and R^2 for each test run. Table 12 shows that the identified models describe the pitch and yaw moment coefficients very well ($R^2 > 90\%$) with low fit error. The body Y-force and Z-force coefficients are not as well described. However, the MSFE for C_Y and C_Z are only slightly greater than the MSFE for C_m and C_n.

Table 12. Mean Squared Fit Error (MSFE) and coefficient of determination (R^2) describing the model fits for C_m, C_n, C_Y, and C_Z.

Test	C_m MSFE	R^2	C_n MSFE	R^2	C_Y MSFE	R^2	C_Z MSFE	R^2
1^a	0.003	91.1	0.001	97.9	0.002	95.2	0.001	95.4
2^a	0.001	97.9	0.001	97.6	0.001	95.9	0.001	96.7
3^a	0.002	96.0	0.001	97.4	0.004	82.0	0.003	91.0
$3b^b$	0.002	94.2	0.001	96.7	0.003	84.9	0.003	85.7
4^c	0.002	95.2	0.001	96.0	0.0004	98.0	0.0005	98.1
8^c	0.001	95.7	0.001	93.4	0.002	80.7	0.002	81.2
7^d	0.001	95.5	0.001	95.8	0.002	91.6	0.001	94.0

[a]Stowed-Canard Configuration Analysis Data

[b]Stowed-Canard Prediction Test

[c]Deployed-Canard Configuration Analysis Data

[d]Deployed-Canard Prediction Test

Figures 20-23 display time histories and spectral densities of actual data, model predictions, and residuals for C_m, C_n, C_Y, and C_Z for the stowed-canard and deployed-canard configurations. The data used in Figures 20-23 was collected from test runs that were not used to determine parameter estimates (Tests 3b and 7 in Table 12).

Figures 20 and 22 show how well the C_m and C_n models fit the data as indicated in Table 12 for the stowed and deployed canard configurations. Notice that the residuals have higher frequency and much smaller values in the time domain plots. The spectral densities show that the models account for the main frequency content. The spectral density of the residuals is small and nearly flat indicating that the remaining residuals may be just noise.

Figures 21 and 23 display time histories and spectral densities of the C_Y and C_Z for the stowed and deployed canard predication cases. As indicated in Table 12, the model fits for C_Y and C_Z are not as good as the fits for for the pitch and yaw moment coefficients discussed earlier. The larger residuals seen in the time history plots may indicate missing signal content in the data. The spectral densities plot show that models still account for the main frequency content of the actual data.
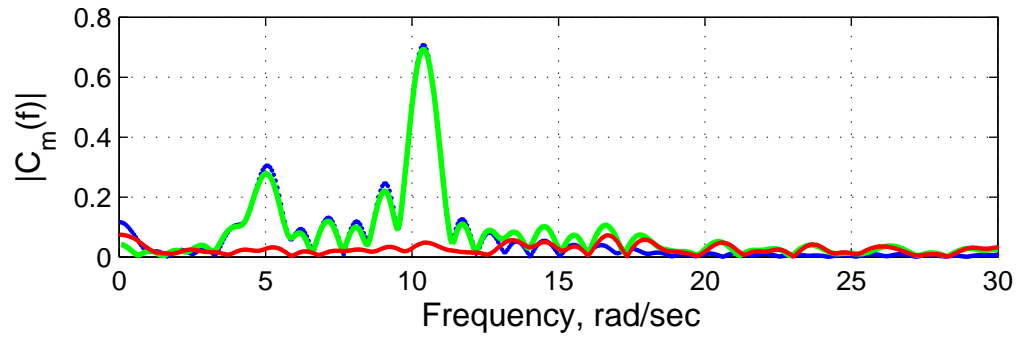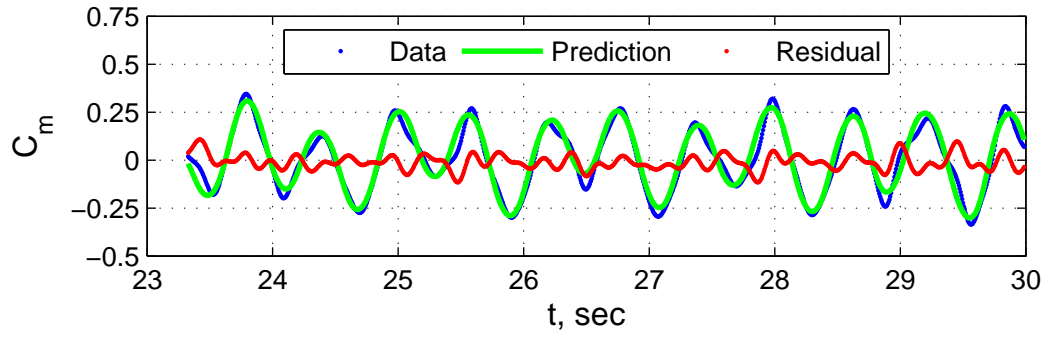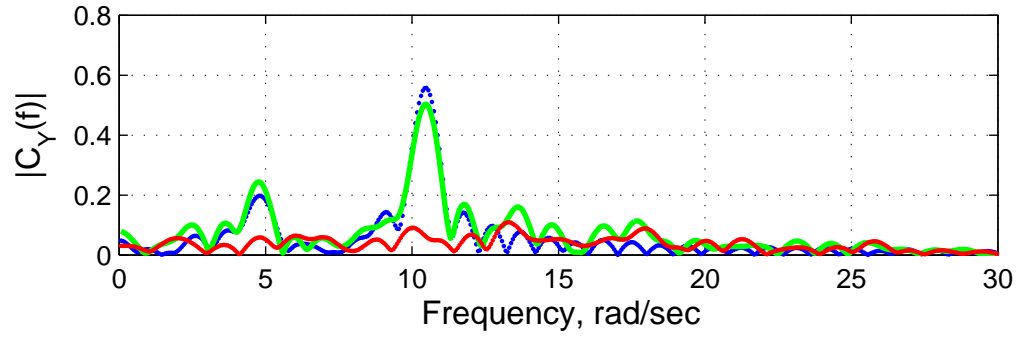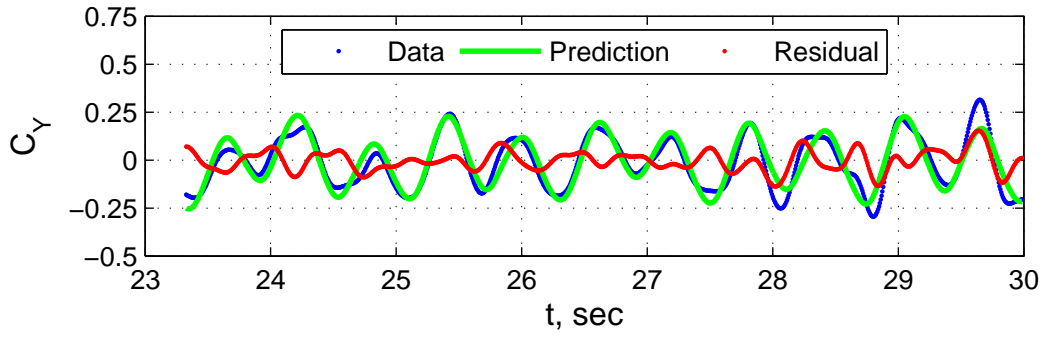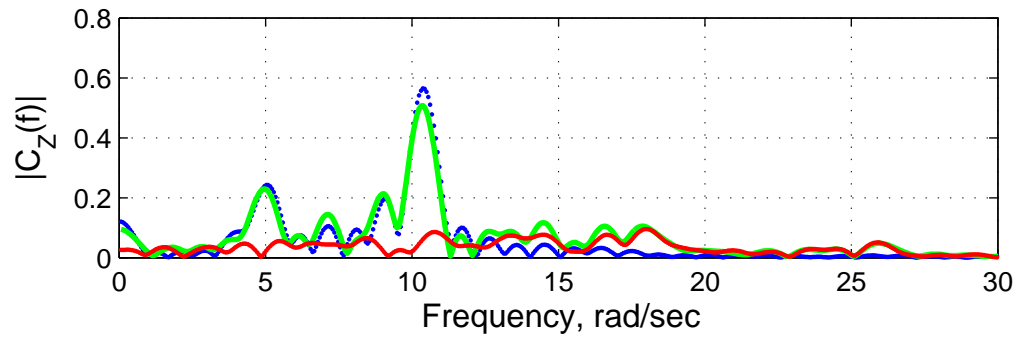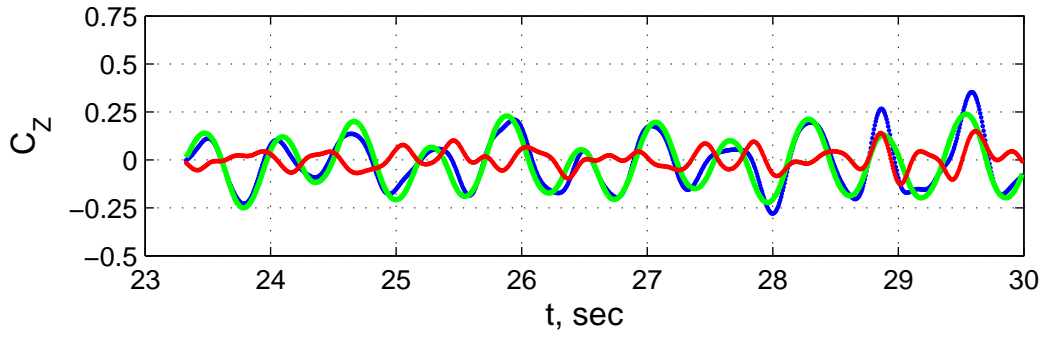
(a) Pitching Moment Coefficient
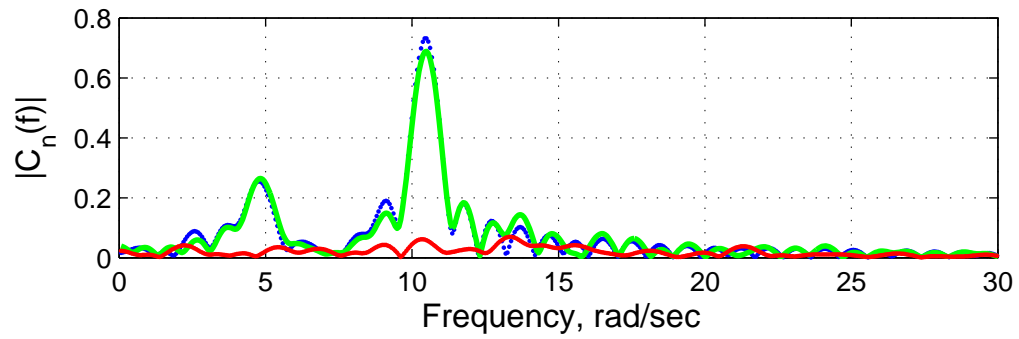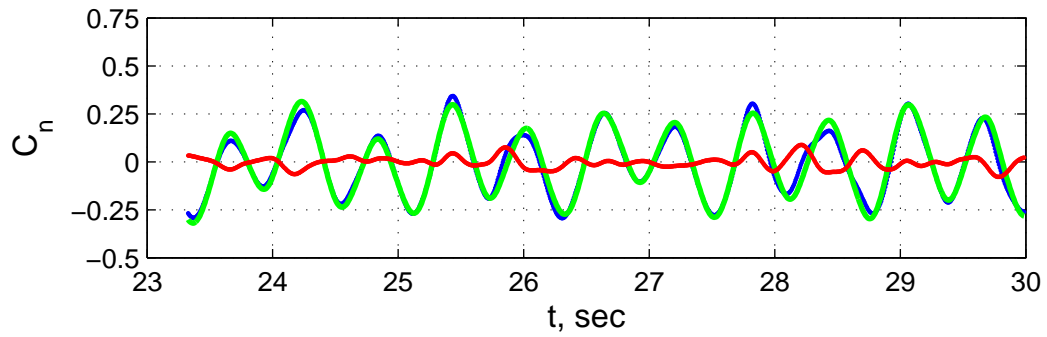
(b) Yawing Moment Coefficient

Figure 20. Moment coefficient predications for the stowed-canards configuration.
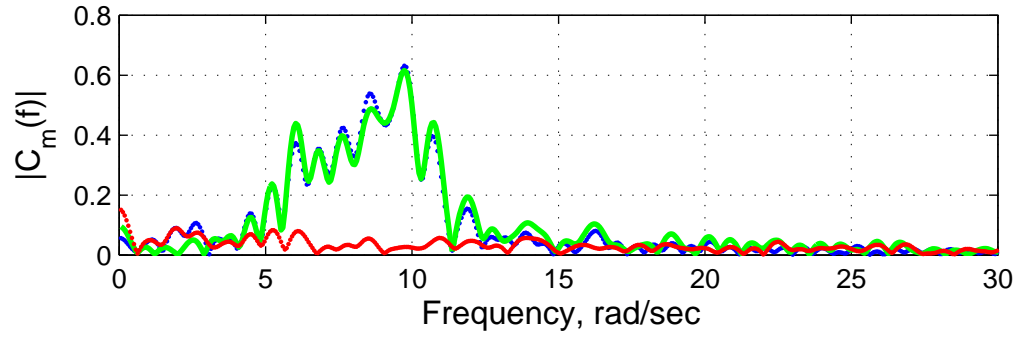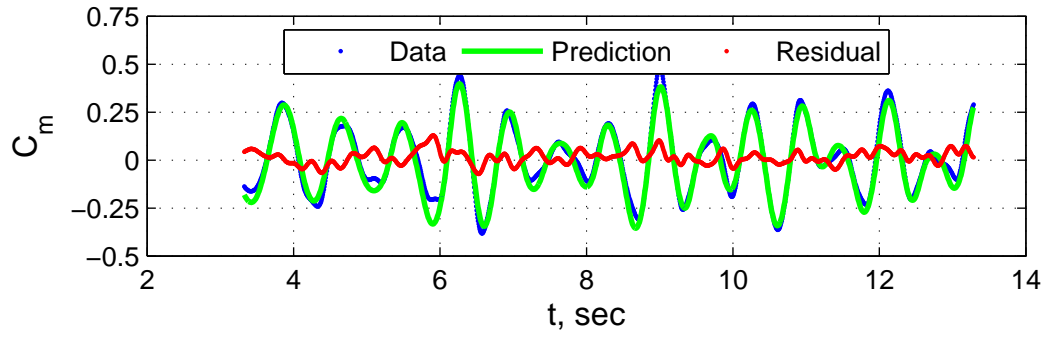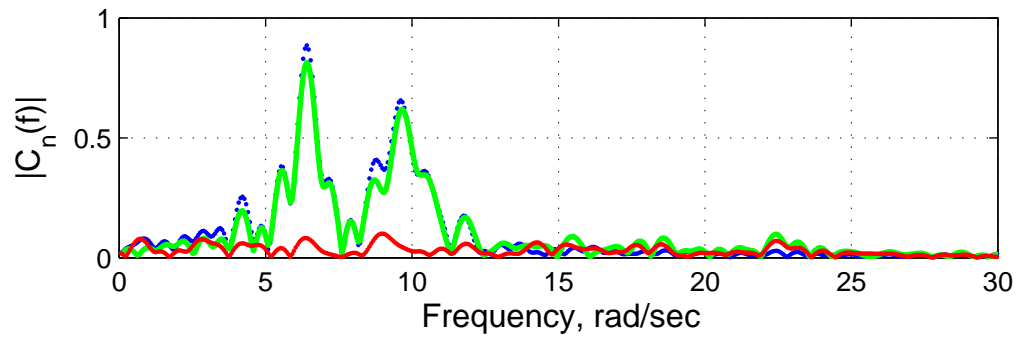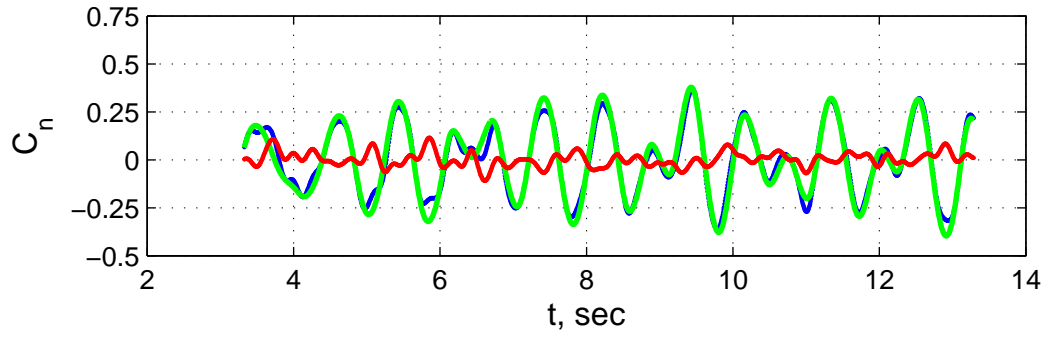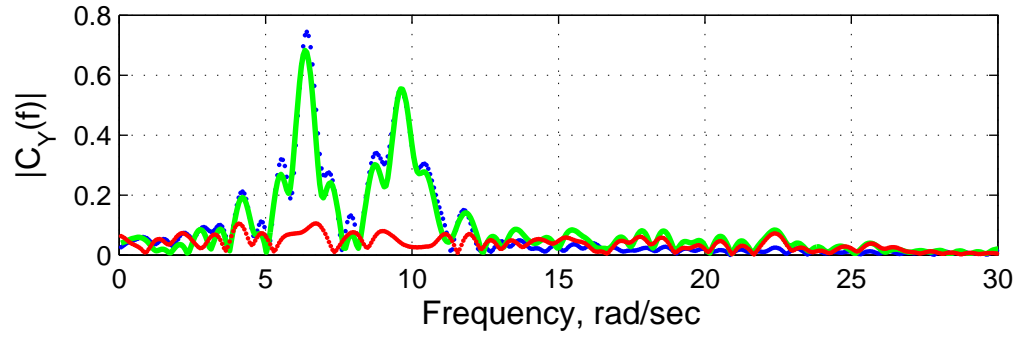
27

(a) Y-Force Coefficient

(b) Z-Force Coefficient

Figure 21. Force coefficient predictions for the stowed-canard configuration.
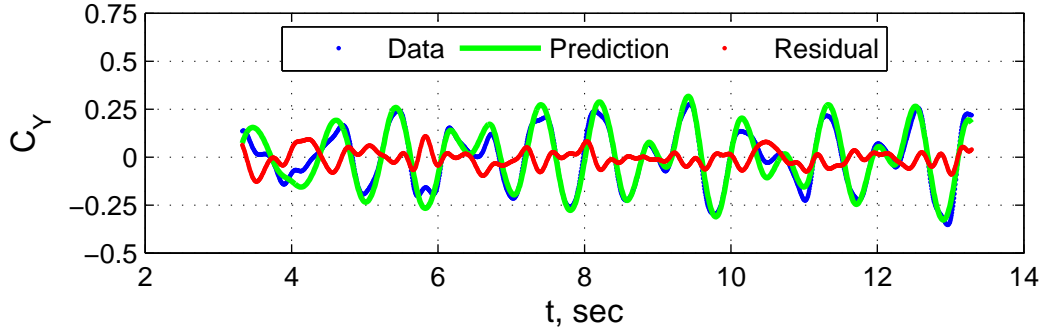
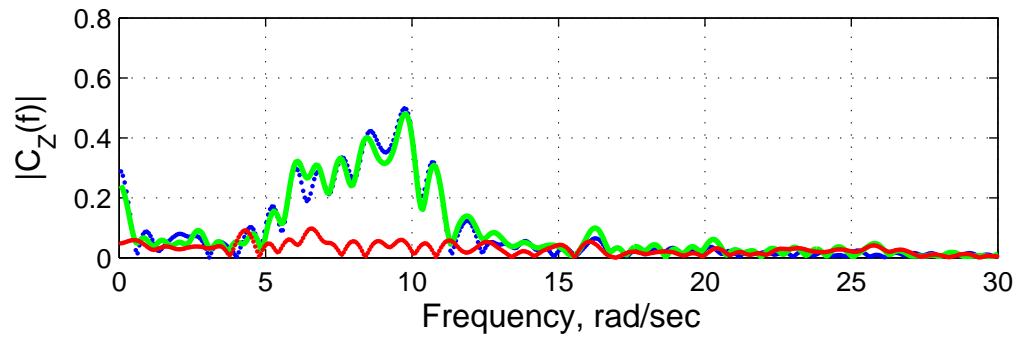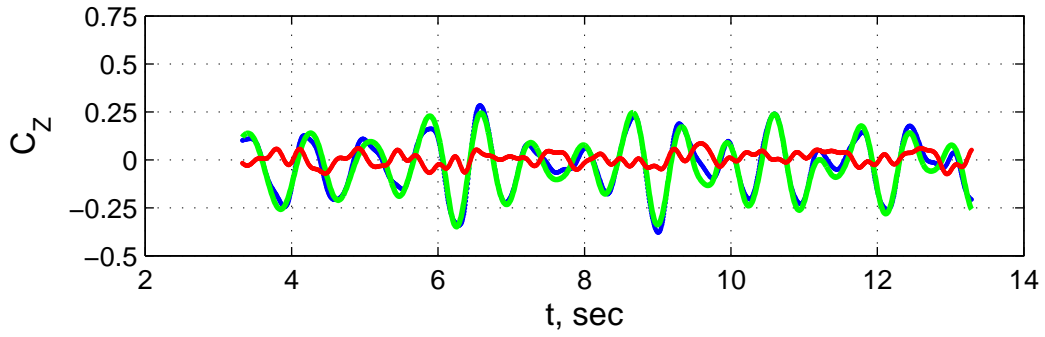(a) Pitching Moment Coefficient

(b) Yawing Moment Coefficient

Figure 22. Moment coefficient predications for the deployed-canards configuration.

(a) Y-Force Coefficient

(b) Z-Force Coefficient

Figure 23. Force coefficient predictions for the deployed-canard configuration.

5   Summary

A free-flight experiment concerning the Launch Abort Vehicle was conducted in the NASA Langley Research Center 20-ft Vertical Spin Tunnel. The goal of the experiment is to understand the aerodynamic characteristics of the Launch Abort Vehicle in the subsonic, incompressible flow regime. This regime represents a portion of the flight trajectory that the Launch Abort Vehicle experiences during the pad abort scenario. Two model configurations were flown during the experiment to determine how canards would impact the aerodynamic characteristics of the LAV.

The primary objective of this experiment is the modeling of the aerodynamic pitch and yaw moments to determine static and dynamic stability of the Launch Abort Vehicle. Models were obtained for the pitch and yaw moments which indicate that the LAV is statically stable longitudinally and directionally in the heat shield forward flight state. Data analysis was unable to determine the longitudinal or directional dynamic stability parameters of the LAV. Models obtained for the canards show a change in trim angle to 174 degrees from 180 degrees when no canards are deployed.

Secondary objectives for the experiment included modeling aerodynamic forces and roll moment acting on the Launch Abort Vehicle. Models were obtained for the force coefficients acting in the body y- and z-directions. Models were not identified for the body x-direction force coefficient and the rolling moment coefficient.

References

1. Bush, G. W., "A Renewed Spirit of Discovery," Office of the Press Secretary, January 2004., Fact Sheet.

2. Stanley, D. and et al, "NASA's Exploration Systems Architecture Study: Final Report," TM 2005-210462, NASA, November 2005.

3. Blanchard, Jr, W. S. and Raper, J. L., "Full-Scale Flight Test From Sea Level of an Abort-Escape System for a Project Mercury Capsule." TM X-422, NASA, October 1960.

4. Moseley, Jr, W. C. and Hondros, J. G., "Aerodynamic Stability Characteristics of the Apollo Launch Escape Vehicle." TN D-3964, NASA, June 1967.

5. Morelli, E. A. and Klein, V., "Application of System Identification to Aircraft at NASA Langley Research Center," *Journal of Aircraft*, Vol. 42, No. 1, January-February 2005, pp. 12–25.

6. Rowland, L. and Jacobs, P., "The Langley 20-Foot Vertical Spin Tunnel Brochure." http://windtunnels.larc.nasa.gov/facilities_updated/flight_dynamics/20foot.htm, October 2006.

7. Bowman, Jr, J. S., "Dynamic Model Tests at Low Subsonic Speeds of Project Mercury Capsule Configurations with and without Drogue Parachutes." TM X-459, NASA, February 1961.

8. Lee, H. A., Costigan, P. J., and Bowman, Jr, J. S., "Dynamic-Model Investigation of 1/20-Scale Gemini Spacecraft in the Langley Spin Tunnel." TN D-2191, NASA, May 1964.

9. Lee, H. A. and Burke, Jr, S. M., "Low-Speed Dynamic Model Investigation of Apollo Command Module Configurations in the Langley Spin Tunnel." TN D-3888, NASA, August 1967.

10. Fremaux, C. M. and Johnson, R. K., "Subsonic Dynamic Stability Tests of a Sample Return Entry Vehicle." Tech. Rep. 20060045567, NASA LaRC, 1999.

11. Mitcheltree, R. A. and Fremaux, C. M., "Subsonic Dynamics of Stardust Sample Return Capsule." TM 110329, NASA, March 1997.

12. Mitcheltree, R. A., Wilmoth, R. G., Cheatwood, F. M., Brauckmann, G. J., and Greene, F. A., "Aerodynamics of Stardust Sample Return Capsule." *Journal of Spacecraft and Rockets.*, Vol. 36, No. 3, May-June 1999.

13. Yates, L. A. and Chapman, G., "Analysis of Data from the Vertical Wind Tunnel of the Mars SRC Vehicle." Final Report PO L-12763, AerospaceComputing, Inc., January 2001.

14. Cahen, G. L., "Effects of Shape and Mass Properties on Subsonic Dynamics of Planetary Probes." *Journal of Spacecraft and Rockets.*, Vol. 12, No. 8, August 1975.

15. Marte, J. e. and Weaver, R. W., "Low Subsonic Dynamic-Stability Investigation of Several Planetary-Entry Configurations in a Vertical Wind Tunnel (Part 1)." TR 32-743, JPL, May 1965.

16. Mitcheltree, R. A., Fremaux, C. M., and Yates, L., "Subsonic Static and Dynamic Aerodynamics of Blunt Entry Vehicles," Tech. Rep. 99-1020, AIAA, 1999.

17. Wolowicz, C. H., Bowman Jr, J. S., and Gilbert, W. P., "Similitude Requirements and Scaling Relationships as Applied to Model Testing." TP 1435, NASA, August 1979.

18. Fremaux, C. M., "Final Report for CEV Test 45-AD: Low Subsonic Dynamic Stability Test of the Orion Launch Abort Vehicle (LAV)," Final Report EG-CAP-07-100, NASA, 2007.

19. Jones, T. W. and Lunsford, C. B., "A Photogrammetric System for Model Attitude Measurement in Hypersonic Wind Tuunels," *Aerospace Sciences Meeting and Exhibit*, No. 2007-1164, AIAA, 2007.

20. Geodetic, "The Basics of Photogrammetry," Geodetic Systems, inc., November 2008, http://www.geodetic.com/info.asp?whatis.

21. Morelli, E. A., "Practical Aspects of the Equation-Error Method for Aircraft Parameter Estimation." *Atmospheric Flight Mechanics Conference and Exhibit*, No. 2006-6144, AIAA, August 2006.

22. Klein, V. and Morelli., E. A., *Aircraft System Identification: Theory and Practice.*, AIAA Education Series., Reston, VA., 2006.

23. Meirovitch., L., *Methods of Analytical Dynamics.*, Dover, Mineola, NY., 1998.

24. Ginsberg, J. H., *Advanced Engineering Dynamics.*, Cambridge University Press., New York, NY., 2nd ed., 1998.

25. Schaub, H. and Junkins., J. L., *Analytical Mechanics of Space Systems.*, AIAA Education Series., Reston, VA., 2003.

26. Henderson, D. M., "Euler Angles, Quaternions, and Transformation Matrices - Working Relationships." JSC 12960, NASA, July 1977.

27. Tolson, R. H., "Space Flight Guidance, Navigation, and Control." NCSU Course Notes for MAE 589., 2007.

28. Owens, D. B., "27-AD Subsonic-Transonic Launch Abort Vehicle Dynamic Stability Test in the NASA LaRC Transonic Dynamics Tunnel," Tech. Rep. EG-CAP-08-79, CEV Aerosciences Project, June 2009.

REPORT DOCUMENTATION PAGE

1. REPORT DATE *(DD-MM-YYYY)*	2. REPORT TYPE	3. DATES COVERED *(From - To)*
01-08-2010	Contractor Report	

4. TITLE AND SUBTITLE

Modeling the Launch Abort Vehicle's Subsonic Aerodynamics from Free Flight Testing

5a. CONTRACT NUMBER

NNL09AA00A

5b. GRANT NUMBER

5c. PROGRAM ELEMENT NUMBER

6. AUTHOR(S)

Hartman, Christopher L.

5d. PROJECT NUMBER

5e. TASK NUMBER

5f. WORK UNIT NUMBER

432938.11.01.07.43.16.01

7. PERFORMING ORGANIZATION NAME(S) AND ADDRESS(ES)

NASA Langley Research Center   National Institute of Aerospace
Hampton, VA 23681-2199   Hampton, VA 23666

8. PERFORMING ORGANIZATION REPORT NUMBER

9. SPONSORING/MONITORING AGENCY NAME(S) AND ADDRESS(ES)

National Aeronautics and Space Administration
Washington, DC 20546-0001

10. SPONSOR/MONITOR'S ACRONYM(S)

NASA

11. SPONSOR/MONITOR'S REPORT NUMBER(S)

NASA/CR-2010-216837

12. DISTRIBUTION/AVAILABILITY STATEMENT

Unclassified - Unlimited
Subject Category 05
Availability: NASA CASI (443) 757-5802

13. SUPPLEMENTARY NOTES

Langley Technical Monitor: Carey S. Buttrill

14. ABSTRACT

An investigation into the aerodynamics of the Launch Abort Vehicle for NASA's Constellation Crew Launch Vehicle in the subsonic, incompressible flow regime was conducted in the NASA Langley 20-ft Vertical Spin Tunnel. Time histories of center of mass position and Euler Angles are captured using photogrammetry. Time histories of the wind tunnel's airspeed and dynamic pressure are recorded as well. The primary objective of the investigation is to determine models for the aerodynamic yaw and pitch moments that provide insight into the static and dynamic stability of the vehicle. System IDentification Programs for AirCraft (SIDPAC) is used to determine the aerodynamic model structure and estimate model parameters. Aerodynamic models for the aerodynamic body Y and Z force coefficients, and the pitching and yawing moment coefficients were identified.

15. SUBJECT TERMS

Orion; Launch Abort Vehicle; System identification; Vertical Spin Tunnel; Subsonic; Aerodynamics; Blunt body

16. SECURITY CLASSIFICATION OF:			17. LIMITATION OF ABSTRACT	18. NUMBER OF PAGES	19a. NAME OF RESPONSIBLE PERSON
a. REPORT	b. ABSTRACT	c. THIS PAGE			STI Help Desk (email: help@sti.nasa.gov)
U	U	U	UU	47	19b. TELEPHONE NUMBER *(Include area code)* (443) 757-5802